INTEGRATED MICRO FUEL CELLS WITH ON-BOARD HYDRIDE REACTORS AND AUTONOMOUS CONTROL SCHEMES

BY

VIKHRAM VILASUR SWAMINATHAN

THESIS

Submitted in partial fulfillment of the requirements
for the degree of Master of Science in Mechanical Engineering
in the Graduate College of the
University of Illinois at Urbana-Champaign, 2011

Urbana, Illinois

Adviser:

Professor Mark A. Shannon

Abstract

Miniaturization of power generators to the MEMS scale, based on the hydrogen-air fuel cell, is the object of this research. The micro fuel cell approach has been adopted for advantages of both high power and energy densities. On-board hydrogen production/storage and an efficient control scheme that facilitates integration with a fuel cell membrane electrode assembly (MEA) are key elements for micro energy conversion. Millimeter-scale reactors (ca. 10 μL) have been developed, for hydrogen production through hydrolysis of CaH_2 and $LiAlH_4$, to yield volumetric energy densities of the order of 200 Whr/L. Passive microfluidic control schemes have been implemented in order to facilitate delivery, self-regulation, and at the same time eliminate bulky auxiliaries that run on parasitic power. One technique uses surface tension to pump water in a microchannel for hydrolysis and is self-regulated, based on load, by back pressure from accumulated hydrogen acting on a gas-liquid microvalve. This control scheme improves uniformity of power delivery during long periods of lower power demand, with fast switching to mass transport regime on the order of seconds, thus providing peak power density of up to 391.85 W/L. Another method takes advantage of water recovery by backward transport through the MEA, of water vapor that is generated at the cathode half-cell reaction. This regulation-free scheme increases available reactor volume to yield energy density of 313 Whr/L, and provides peak power density of 104 W/L. Prototype devices have been tested for a range of duty periods from 2–24 hours, with multiple switching of power demand in order to establish operation across multiple regimes. Issues identified as critical to the realization of the integrated power MEMS include effects of water transport and byproduct hydrate swelling on hydrogen production in the micro reactor, and ambient relative humidity on fuel cell performance.

To Father and Mother.

Acknowledgments

I am extremely fortunate to be pursuing my graduate research under the advise of Prof. Mark Shannon. To have gotten the opportunity to work on MEMS, a topic close to my heart, is a dream come true. Prof. Shannon, along with Prof. Rich Masel, made the Micro Fuel Cell Project possible and this has been the heart of my MS thesis. During the course of this work, I have learned several things from my adviser—on the art of conducting research, communication, advising and teaching and, most importantly, ethics. While Mark often jokes about giving me a hard time during group meetings, this has single handedly molded my presentation skills. Mark has been extremely supportive and encouraging throughout, even through difficult times. My work would not have made it to IEEE MEMS without the encouragement of my advisers. I would also like to thank the Defense Advanced Research Project Agency and the MechSE Department for financial support.

Dr. Likun Zhu, post-doc at the time and now faculty at IUPUI, was my close mentor throughout my MS. I am extremely indebted to him for guiding me through my infancy in MEMS and experimentation. While on one hand he had such a patient attitude towards me, he gave me complete freedom and intellectual space to explore my ideas and was always by my side throughout this work. I learnt most about fuel cells from Dr. Bogdan Gurau, and tips and tricks in microfabrication from Dr. Byunghoon Bae and Dr. Junghoon Yeom. MEMS and fuel cell reserach would not have been fun without the likes of my senior colleagues.

Dr. Bruce Flachsbart gave me my first real lessons in MEMS and some of the best about clean-room research. I continue to work closely under his advise, and also as a TA. Thanks to Dr. Glennys Mensing, who has provided much support and coordinated my research, besides guiding me through my TAs. Prof. Pratap Vanka and Dr. Richard Keane with whom I've had several useful discussions and my first lessons on tutoring. I am also extremely grateful to Kathy Smith, Laura Herriott and Laurie Macadam, who have offered me much support on behalf of the MechSE department, especially with my travel and visa issues. And my peers of Shannon group, who have given me so many ideas and suggestions along the way.

Academics aside, I am very glad to have found the most wonderful friends at Champaign-Urbana. Dr. Anjan Raghunathan, Vijay Raman and Gayathri Mohan have helped me so much with settling in to the U of

I. And the likes of Aravind, Vidisha, Harini, Gowri, Kaushik, Pradeep, Praveen, Vinay, Milu, Vivek, Raghu, Avanija, Navaneethan, Swetha, Vinod, Chandu and Preeti, for putting up with several of my quirks, with whom I shared the best of times over tea, games and debates.. and who also got me to run the Chicago Marathon in the meantime!

Last but not the least—my parents, Uma and Swaminathan, little brother, Rohith, and family! They have been the greatest source of inspiration throughout my pursuits. I have always found their advise and philosophy to fall back on whenever I needed help to maintain focus and motivation. While they have quietly been my emotional support throughout indefinite wait times over travel, they haven't for once been short of encouragement. Although this thesis has taken some time shaping up, I dedicate it to my parents. And to Yamini, for being with me all along.

Table of Contents

List of Tables

List of Figures

List of Abbreviations

MEMS	Micro-Electro-Mechanical Systems.
MEA	Membrane Electrode Assembly.
FC	Fuel Cell.
RFID	Radio-frequency identification.
EDL	Electrochemical Double Layer.
PEMFC	Proton Exchange Membrane Fuel Cell.
DMFC	Direct Methanol Fuel Cell.
FAFC	Formic Acid Fuel Cell.
AFC	Alkaline Fuel Cell.
PEM	Proton Exchange Membrane.
ORR	Oxygen Reduction Reaction.
SS	Stainless Steel.
IPA	Isopropyl alcohol/propan-2-ol.
MOF	Metal-organic framework.
PI	Polyimide.
PDMS	Polydimmethylsiloxane.
EDM	Electrical Discharge Machining.
ICP-DRIE	Inductively Coupled Plasma-Deep Reactive Ion Etching.
SC-1	Standard Clean-1.
RIE	Reactive Ion Etching.
DI water	Deionized water.
PTFE	Polytetrafluoroethylene.
WRMFC	Water Recovery Micro Fuel Cell.

List of Symbols

t	Membrane thickness.
a	Membrane radius.
r	Radius of infinitesimal ring element.
$w(r)$	Deflection, as a function of radius.
w_o	Membrane center delfection.
w_{max}	Membrane maximum delfection.
ds	Elemental arc length.
ϵ_r	Differential elemental strain.
$\epsilon_{r,max}$	Maximum elemental strain.
ϵ_a	Mean strain.
ΔP	Pressure difference.
E	Young's modulus.
ν	Poisson ratio.
σ_o	Tensile strength.
r_1, r_2	Radii of curvature of meniscus.
ϕ	Solid-liquid contact angle.
h	Channel height.
w	Channel width.
dA	Surface area of meniscus element.
$d\theta_1, d\theta_2$	Angles subtended by elemental meniscus at center of curvature.
σ	Surface tension.
U_σ	Surface energy due to surface tension.
F_x	Surface tension pumping force.
$w'(x)$	Rate of channel width change with respect to length.
κ	Meniscus curvature.

Chapter 1

Introduction

1.1 The state of the art in microscale power generation

Microsystem technology, tapping the advantages of miniaturization science, has led to the development of electromechanical systems of smaller sizes yet increasingly sophisticated capabilities. In the process, the energy needs of these systems have increased with complexity and are also having to pack to greater densities for size reduction. In order to power up and automate fully functional wireless sensors, bio-MEMS, micro-robots, RFID tags etc., it is essential for their on-board power sources to miniaturize too! A micro power source must have the capability to cater to systems of a wide gamut of operating lifetimes (time scales of hours-to-days-to-years), and also meet peak demands (1 mW) in short bursts. Several methods have been explored for power generation at the microscale:

a) Micro fuel cells [1], [2], that store energy in highly concentrated chemical form and release it on-demand. Such devices have an inherently high conversion efficiency and are particularly favorable for the microscale because of their ability to simultaneously deliver high energy density and power density of 100mW/cm^2. Their performance is limited, typically, by the supply and concentration of the fuels.

b) Micro energy harvesting devices, that passively extract energy from surrounding vibrations, heat etc. Such devices have potentially infinite lifetimes but very low power density ($\leq$1 μW/cm^2). Fully automatic, self-winding wrist watches are classic examples of energy harvesting.

c) Microbatteries, that use rechargeable solid state electrode/electrolyte materials to store energy when charged and release it on demand. While they can have high energy density, they typically have low power density in such regimes (button cells in watches that operate at trickling power loads for years, for example). High capacity and power density lithium-ion and lithium-polymer electrode materials are currently being developed [3], [4], but the energy and power density at the device level can be drastically reduced by volumetric demand from supporting substrates and charge collection layers.

d) Ultracapacitors, that use high surface area to store energy in electrochemical double layers (EDLs). Such

devices can deliver at very high power densities, given the short charge transport distances (of the order of nm), and are good candidates as boosters in micro power generators. Their energy density, however, is low and life cycles are too short for extended operation.

Given the inability of ultracapacitors to scale up for bulk energy density and micro energy harvesting devices to concentrate into higher power densities, the microbatteries and micro fuel cells have been favored. While on one hand the microbattery is increasingly strained to simultaneously meet both energy and power demands, the micro fuel cell emerges as strong contender for power generation at these dimensions.

Fuel cell research has mostly focused on portable applications [5] that typically operate in the 1-10 W regime, using methods of reforming methanol [6] and other liquid fuels as for ease of storage and supply. However this approach has an impact on the operating efficiency of the fuel cell and limits the capacity, whereas high energy densities are a primary objective of miniaturization. It is rather preferable to use hydrogen/air redox reactions that are more efficient for energy conversion, and seek the integration of high capacity fuels based on chemical hydrogen sources. The motivation is to design and implement such a high capacity micro power generator that takes advantage of favorable phenomena at the micro scale for its operation.

1.2 What are fuel cells?

Fuel cells are electrochemical devices comprising an electrolyte medium, an ion transporting liquid or solid, in contact with two electrodes where redox reactions occur leading to direct conversion of fuel to electricity. Electricity production through this mode is particularly preferred as fuel cells can convert upto 80% of chemical energy, nearly twice the efficiency of other thermal methods that involve mechanical intermediaries (e.g. turbines and generators) accompanied by losses [7]. Furthermore, they are also eco-friendly as the byproducts are typically heat, water and/or carbon dioxide. Although in structure fuel cells resemble batteries, their differences arise from the fact that fuel cells are continuous in operation and perform consistently as long as fuel supply and load are maintained whereas batteries are storage devices and need periodic charging from a primary external source for replenishment of their energy.

Fuel cells are most commonly classified on the basis of the electrolyte, the most commonly used being commercially available Nafion® membrane—a sulphonate ionomer embedded in a Teflon® matrix. Numerous other classification factors also include the nature of ionic species involved, the direction of its transport, the type of fuel processing (external or internal reforming) and operating temperature. At the portable and micro scales, the proton exchange membrane fuel cells (PEMFCs) [8],[9], direct methanol fuel cells

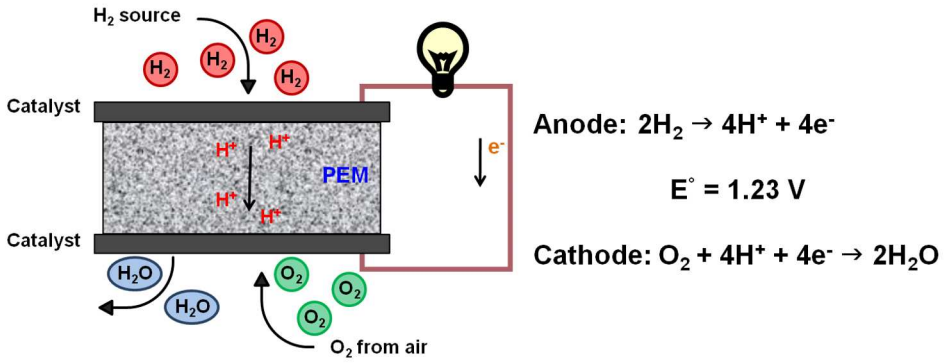

Figure 1.1: Schematic of hydrogen fuel cell operation, showing electrode redox reactions

(DMFCs), formic acid fuel cells (FAFCs) and alkaline fuel cells (AFCs) are favored owing to their ability to operate efficiently in the range of 20°C to 80°C. Among these methods, the PEMFCs have been chosen for miniaturization for the following reasons: *a*) PEMFCs operate with maximum cell voltages and power densities when combined with a hydrogen source of suitable capacity; *b*) DMFCs and FAFCs, despite their high fuel energy content [2], operate at dilute concentrations due to thermodynamic limitations and are often accompanied by issues of carbon monoxide catalyst poisoning [10]; *c*) DMFCs, FAFCs and AFCs require auxilliary transport circuits to remove byproduct carbon dioxide for efficient catalysis, an added complexity in a 10 μL system at the expense of volumetric energy density. *d*) Some uncoventional approaches such as laminar flow fuel cells [11] can operate without the use of membranes, but their slow kinetics and incomplete fuel consumption limit their ability to meet power and energy density requirements.

1.2.1 The hydrogen-air PEMFC

Figure 1.1 shows a schematic representation of a simple hydrogen fuel cell membrane electrode assembly (MEA), along with cell reactions. The device comprises of two catalyst coated electrodes, separated by the ion-selective PEM. H_2 supplied at the anode undegoes oxidation on the catalyst, to produce protons that are transferred across the PEM. The protons combine with O_2 at the cathode in a reduction reaction to produce water. Due to the selectivity of the PEM, the electrons required for the reduction reaction are forced to transport externally and the associated current can be drawn by ohmic load in the circuit to extract electrical energy. The theoretical open circuit voltage for the cell reactions is 1.23 V, but unavoidable losses associated with mixed potentials and partial catalyst oxidation limit this in practice to about 1 V. Figure 1.2 shows the characteristic polarization behavior of a hydrogen fed fuel cell [12]. The curve is split into thee distinct regimes:

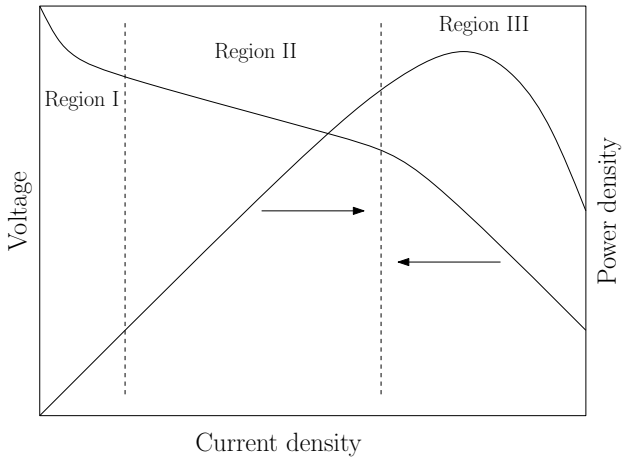

Figure 1.2: Typical polarization behavior of a hydrogen fuel cell

a) Region I, where the fuel cell operates at low power demand with high voltages and low current densities close to the open circuit limit. In this regime, the performance is governed by the activation potentials of the oxygen reduction reaction (ORR) at the cathode. While this is closest to equilibrium conditions for maximum thermodynamic efficiency, the voltage-current density delivery changes sharply.

b) Region II, after the losses of activation potential where the behaviour is pseudo-linear. In this region, the linear IR drop observed is due to ohmic losses arising from internal resistance of the PEM and other components of the fuel cell.

c) Region III, with mass transport limited performance. At high current density, rapid catalysis occurs at the electrodes in order to meet the power demand but the fuel cell is limited by the sluggish kinetic of ion transfer across the PEM.

A favorable point for operationg the fuel cell, for maximizing efficiency with adequate power delivery, occurs in the transition between regions I and II with switching to region III during periods of high power density requirement. The actual voltage and current at which the fuel cell operates is determined by electrical load. The MEA is said to function as long as stable supply of H_2 and O_2 is maintained, along with a load-based control.

1.3 Thesis outline

The objective of this project has been to develop prototype micro fuel cells that combine such an efficient MEA and a hydrogen generator, operated by passive microfluidic control schemes. The design goal for

the micro power generator, of ca. 10 μL size, has been to pack an energy density of 200 Whr/L over an operating lifetime of several hours along with the ability to meet a sustained peak power density requirement of 100 W/L. At the microscale, battery technology has been demonstrated to provide high energy density when operated in low power regimes; however, the micro fuel cell system merits from its ability to combine both high energy and power densities and supply at rates that track variations in electrical load. In this thesis, the evolution from-concept-to-reality of this miniaturized system is presented in three parts. Chapter 2 discusses miniaturization issues while describing integration of the two primary components of the device–the MEA, and the on-board fuel itself. The next two chapters deal with working characteristics of this micro fuel cell system and the design of its control scheme. Chapter 3 proposes the integration of a fully passive microfluidic control layer, using a surface tension pumping channel with a microvalve. In Chapter 4, an alternate approach to hydrogen generation is proposed, by back diffusion of water vapor from the cathode to the microreactor through the PEM. While this method seeks to increase energy density by eliminating the control layer and on-board water storage, governing parameters and limiting factors for this mechanism are analyzed for their impact on micro fuel cell performance. Chapter 5, in conclusion, highlights the significant developments and outcomes of this study and projects an outlook for the future of micro fuel cell power generation.

Chapter 2

Miniaturizing the MEA and integrating a hydrogen source

2.1 Aspects to miniaturization

A micro fuel cell may be visuallized as constituted by three distinct sub-systems– the MEA, an on-board fuel and the fluidic/control circuits. Large-scale fuel cell systems rely heavily on complex, bulky controls to manage current generation. Their MEAs may be multiply stacked and their size warranting complex fluidic schemes for thermal management [7]. A favorable effect of miniaturizing an MEA is that the heating problem is offset by surface area-to-volume scaling as we are able to dissipate away excess heat with relative ease. While it has been shown at the large scale that Nafion-based PEMFCs operate best at a temperature of 80°C, operating our system at room temperature minimizes thermal losses and requires much less thermal management. On one hand, this simplifies the microfluidic control circuits; we also demonstrate further how such simplified schemes, while they occupy less volume, improve system performance by better water management in the MEAs from ambient humidity. Decreasing the size of the MEA and auxilliary real estate enables us to gain on energy density by accommodating a greater volume fraction of fuel.

The choice of a suitable fuel for a micro fuel cell system departs from criteria that dictate fuel sources for large fuel cells. At the large scale, the constraining metric on a fuel is its gravimetric hydrogen density, the cost of storing the fuel is dictated by weight considerations. In the micro scale, however, the paradigm shift occurs because our ability to design and produce devices is better dictated by volumetric limitations than by mass. Hence, the thrust is to develop and package such fuels that have high capacity for *hydrogen-per-unit-volume* than *hydrogen-per-unit-mass*. Liquid hydrogen (leakage hazard and handling issue aside) may not necessarily be the highest capacity source at these scales, as we discuss in section 2.3.1.

In this chapter, we present miniaturized versions of the MEA and the fuel source that have been scaled down for a ca. 10 μL system, along with performance metrics. The following two chapters discuss control schemes and present integrated prototype devices along with their experimental performance characteristics.

2.2 Membrane Electrode Assembly

2.2.1 Fabrication

The miniaturized MEA (figure 2.1) was made by sandwiching Nafion® 112 polymer electrolyte between two 25 μm thick stainless steel (SS) sheets, each having a laser-cut square window of 1/4 mm^2. The layers were stacked and bonded via an epoxy adhesive transfer process [13], as outlined in section 3.4.1. Catalyst ink (a suspension of Pt-black and carbon powder in isopropyl alcohol) was painted directly onto the PEM square windows on either side, adequately contacting the SS sheet, in order to create electrodes. A 50 μm thick SS spacer was bonded around the MEA using 3-M 2216^{TM} two-part epoxy resin.

2.2.2 MEA performance

A miniature-scale 4 mm^2 MEA when tested at room temperature for performance, using dry hydrogen at the anode supplied from a tank and quiescent air breathing cathode, operated at open cell voltage of 0.99 V and supplied peak power density of over 200 W/cm^2 (figure 2.2). A comparison of a similarly assembled 1 mm^2 MEA with other silicon-based microfabricated fuel cell systems is shown in table 2.1[1]. The miniaturized MEA showed enhanced performace (improved open circuit and peak power delivery) over the other approaches, due to improved fraction of active area as well as reduced transport losses in the PEM. The ability to perform with a self-breathing cathode in quiescent, room temperature ambient conditions would enable the design and development of micro power generators using such an MEA.

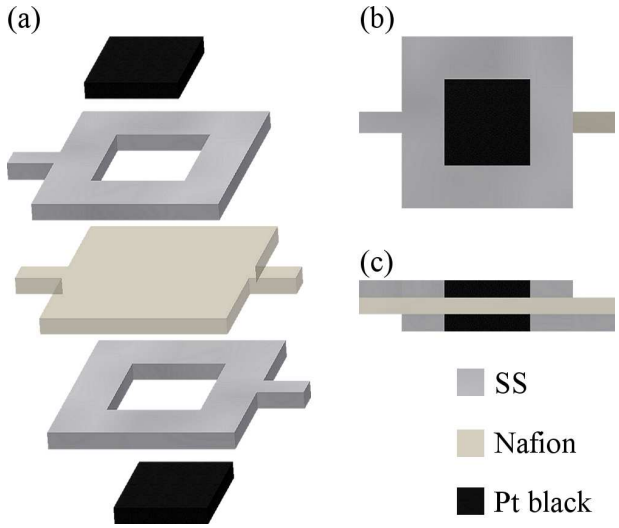

Figure 2.1: Schematic of the MEA, showing (a) assembly, and finished (b) top and (c) side views

[1]Reproduced from Gurau et al. [14], by permission of The Electrochemical Society

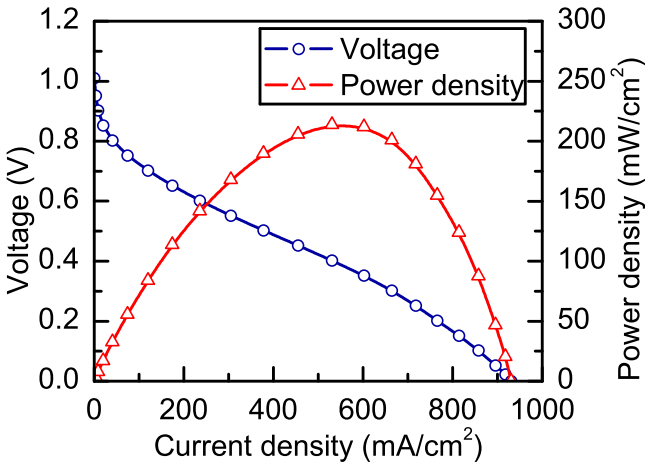

Figure 2.2: Polarization and power density curves for the miniature MEA before integration

	Open Cell Voltage (V)	Cell Area (mm^2)	Design	Peak Power Density (mW/cm^2)
Yu et al. [15]	0.95	500	Si wafers bolted to conventional MEA	195 with pure O_2 flowing on cathode
Modroukas et al. [16]	0.85	100	Si wafers bonded to conventional MEA	70 with flowing air on cathode
Meyers et al. [17]	0.9	Not Given	Si wafers bonded to conventional MEA	63 with pure O_2 flowing on cathode
Yeom et al. [10]	0.95	100	Si wafers bonded to Nafion	35 with stagnant air on cathode
Zhiyong et al. [18]	0.96	123	Si wafers bonded to Nafion	13.7 with pure O_2 flowing on cathode
Pichonat et al [19]	0.8	7	Nafion filled Si MEA	18 with pure O_2 flowing on cathode
This Work [14]	0.95	1	Nafion filled SS MEA	280 with self breathing cathode

Table 2.1: Comparison of the miniature MEA with literature on hydrogen-fed micro fuel cells

2.2.3 Low temperature MEA fabrication

In an alternate approach, the MEA was also prepared by low temperature bonding. The PEM and SS sheets were stacked in a similar manner, but bonded using liquid nafion (dissolved in IPA) under pressure at 80°C on a hotplate. Prior to bonding, the Nafion 211 membrane was conditioned by soaking in sulfuric acid and hydrogen peroxide baths at 80°C for 1 hr each. The catalyst was painted directly onto the bonded PEM as before. We hypothesize two reasons for improvement in MEA performance when fabricated using this process. Lowering the final bonding temperature ensured that pores within the fuel cell membrane retained water and didn't collapse. At temperatures $\geq$120°C, dehydration is known to cause nanopores in Nafion to close, thus leading to poor proton transport. Further, electrical contact between the PEM and the SS sheet

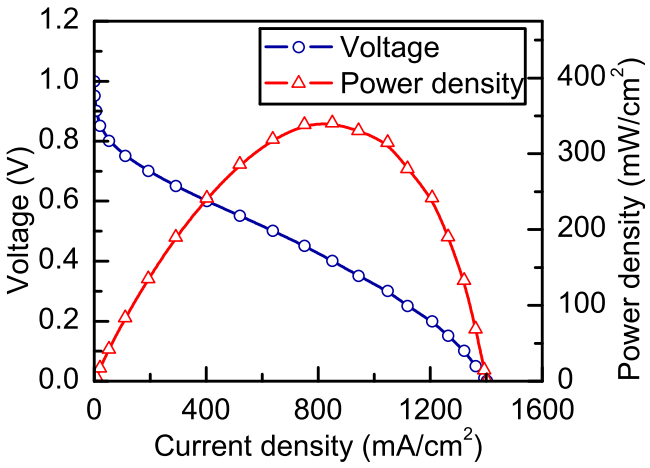

Figure 2.3: Polarization and power density curves for the Nafion-bonded PEMFC

contacts was also expected to improve beacuse of the use of nafion itself instead of an inherently insulating epoxy adhesive. Adhesion strength is much poorer than epoxy bonding as it is mainly based on weak Van-der-waal's forces, and the assembly was found to disintegrate by delamination upon prolonged exposure to extreme humidity. A sample PEM prepared by this process was tested, and its polarization behaviour is shown in figure 2.3. For a 4 mm^2 active area while the open circuit voltage was similar as before at 1.01 V, peak performance showed a two-thirds jump to increase as high as 342 mW/cm^2. Once past the activation regime, at 0.7 V, the current density nearly doubled from ca. 100 mA/cm^2. At 0.2 V, near short-circuit and under mass trasfer limitation, the current density increased by over 50% to exceed 1200 mA/cm^2.

2.3 Hydrogen generation and storage

A high-capacity hydrogen source is required in order to supply fuel to the MEA and maintain power generation. While hydrogen consumption rates at the anode vary greatly with power demand due to external electrical load on the micro fuel cell, the fuel source must be capable of delivering at these rates across various operating regimes in a stable manner. In order to meet energy density requirements, we need to pack sufficiently large quantity of hydrogen per unit volume. For simplicity, direct on-board hydrogen in a pressurized or liquefied form, may appear as an attractive option for maximizing the fuel cell efficiency. However, the small size of the hydrogen molecule causes it to diffuse through most structural materials used in storage systems, making them lossy, besides prone to degradation through embrittlement. Coupled with high flammability, this poses a handling/safety hazard. As a result, it necessitates incorporating hydrogen alternatively in a fuel and releasing through chemical reactions. The kinetics of hydrogen generation/release

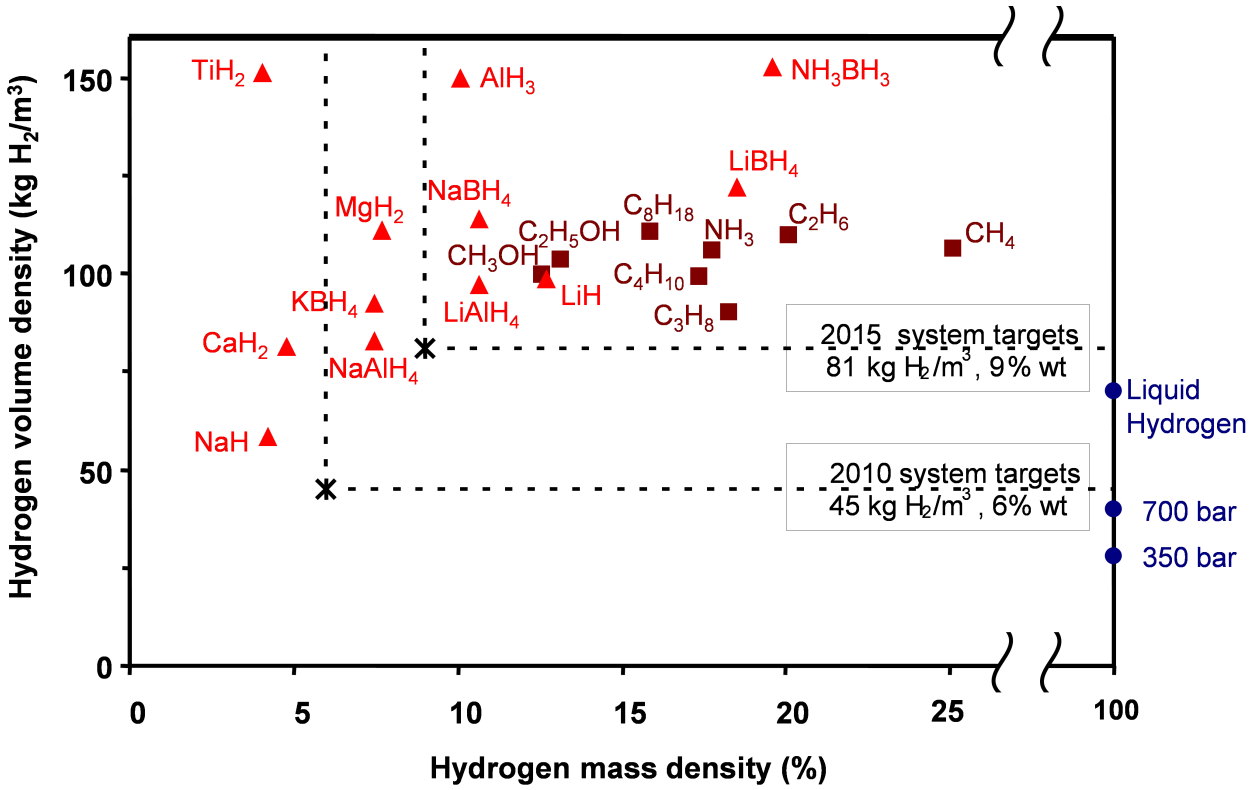

Figure 2.4: Hydrogen release capacity of common chemical sources[2]

from the fuel ultimately determines the power density limits for operating the MEA.

2.3.1 Chemical hydrogen sources for PEMFCs

Numerous chemicals have been proposed in literature as candidate fuels for PEM systems, including inorganic and metal hydrides [21],[22],[23], organic hydrocarbons and low molecular weight alcohols, and sorption media such as carbon nanotubes [24],[25],[26] and metal organic frameworks (MOFs) [27]. Most inorganic hydrides release hydrogen via controlled water or acid hydrolysis reactions, while organic chemicals do so by reforming reactions [6],[28],[29]. MOFs naturally absorb hydrogen and desorb at elevated temperatures. While it is desirable that the chemical have high hydrogen content or storage capacity, the chemical is also expected to release hydrogen spontaneously.

Figure 2.4 shows volumetric and mass density data for available hydrogen, for a number of metal hydrides, organic and a few inorganic sources. Also included are the U.S. Department of Energy's Freedom Car Program stipulated estimates of minimum hydrogen volumetric and mass densities, by the years 2010 and

[2]Reproduced from [20], with permission from Elsevier

2015, for the automotive hydrogen economy [30]. From the figure, while TiH_2 has the highest volumetric density, CH_4 has the greatest mass density and NH_3BH_3 combines both high volumetric and mass density of hydrogen. Hydrocarbons, alcohols and NH_3 have relatively moderate capacities in comparison. However, these fuels suffer from drawbacks associated with the high energetics of hydrogen release and reaction by-products' handling issues. Fuel reforming reactions for methanol and ethanol have been successfully demonstrated at the larger size scales. It is, however, not feasible to miniaturize auxilliary reforming systems and generate hydrogen at high temperatures ($\geq 1000°C$) in a microscale power generator without parasitic power losses. While MOFs have been developed as excellent sources for adsorbing, concentrating and desorbing hydrogen in preconcentrators for portable gas analysis systems [31], the sorption cycles are subject to temperatures over 200°C. Hence the choice of the candidate fuels, while determined by the volumetric and mass density of available hydrogen, is limited by the energetics and temperature of hydrogen production.

2.3.2 Hydrogen generation from metal hydrides

Metal hydrides emerge as the most attractive fuel sources for our system, owing to their spontaneous hydrolysis reactions at room temperature conditions. Within these metal hydrides, the choice of a suitable fuel is governed by *a*) the extent to which hydrolysis reaction proceeds towards completion *b*) the reaction kinetic, which is in-turn influenced by the water-vapor partial pressure, and *c*) solubility and porosity of the soild fuel, both of which depend on the volume expansion of byproduct hydroxide/hydrate. Table 2.2 shows theoretical volumetric hydrogen capacities of metal hydrides, with corrections based on volume expansion of reaction products. The stoichiometric volume of hydrogen has been estimated from bulk mass density of reactants at room temperature. Based on recent experiments to characterize hydrides [32],[33],[34],[35],[36], Calcium Hydride demonstrated superior reaction kinetics and yield. This was attributed to reduced resistance to water vapor diffusion through the porous reaction products, arising from volume expansion, whereas Lithium Hydride formed an agglomerated mass preventing contact between reactants [20]. Lithium Aluminum Hydride is estimated to provide the greatest hydrogen yield owing to the smallest byproduct expansion, and can thus pack the maximum volume of hydrogen on-board the device. From the point of view of miniaturization and volumetric yields, Calcium Hydride (CaH_2) and Lithium Aluminum Hydride ($LiAlH_4$) have been chosen as the fuels for the hydrogen generator. While CaH_2 produces 5% by weight hydrogen and $LiAlH_4$ has nearly double that capacity, the former has faster kinetics due to increased by-product expansion of ca. 50%.

Hydrolysis reactions	H_2 release (H_2/reactants) (mm^3/mm^3)	Volume expansion of byproducts %	H_2 release w/ expansion (mm^3/mm^3)
$LiBH_4 + 4H_2O \longrightarrow H_3BO_3 + LiOH + 4H_2$	934	178%	747
$NaBH_4 + 4H_2O \longrightarrow H_3BO_3 + NaOH + 4H_2$	912	173%	734
$LiH + H_2O \longrightarrow LiOH + H_2$	882	286%	530
$NaAlH_4 + 4H_2O \longrightarrow Al(OH)_3 + NaOH + 4H_2$	846	118%	788
$LiAlH_4 + 4H_2O \longrightarrow Al(OH)_3 + LiOH + 4H_2$	863	117%	815
$CaH_2 + 2H_2O \longrightarrow Ca(OH)_2 + 2H_2$	843	150%	706

Table 2.2: Theoretical hydrogen yield from metal hydrides upon hydrolysis

2.3.3 Design of a microreactor for hydrolysis of metal hydrides

A miniature hydride reactor has been designed for a 10 μL fuel cell system, for studying hydrogen generation reactions using Calcium Hydride. A schematic of this device is depicted in figure 2.5. The hydride reservoir and water chamber have been so designed as to accommodate stoichiometric quantity of water on-board. The shape of the hydrogen generator also accounts for fabrication aspects during device assembly, and provides upto 47% reactor volume for packing the fuel. Considering 50% hydrogen release, by accounting for packing limitations due to powder form factor of the fuel and by-product volume expansion, the estimated hydrogen production for the reactor is 2.54 mL. This corresponds to an energy density of 332 Whr/L upon complete consumption at 0.6 V operation. In comparison, a microreactor was reported in 2003 by Kong et al. [33] that produced hydrogen by hydrolysis of metal hydride powders with water vapor. However the fuel storage (encapsulated in a nickel mesh) being as little as 3% of the entire device volume, it seriously decreased the overall energy density. In our design, the objective has been that of increasing the on-board fuel and water towards maximizing the capacity of the fuel cell.

Experiments were performed for various sizes and configurations of water holes and hydrophilic/hydrophobic membranes in the control layer, in order to determine suitable reaction rates. Test results are depicted in figure 2.6 (all devices had a 0.4 mm hole below the water chamber in the control layer):

blue One 0.3 mm hole underneath hydride chamber covered with hydrophobic membrane on hydride side.

pink Two 0.3 mm holes underneath hydride chamber. Both are covered with hydrophobic membrane on hydride side, and only one hole covered with hydrophilic membrane on the MEA side.

red One 0.8 mm hole underneath hydride chamber covered with hydrophobic membrane on hydride side.

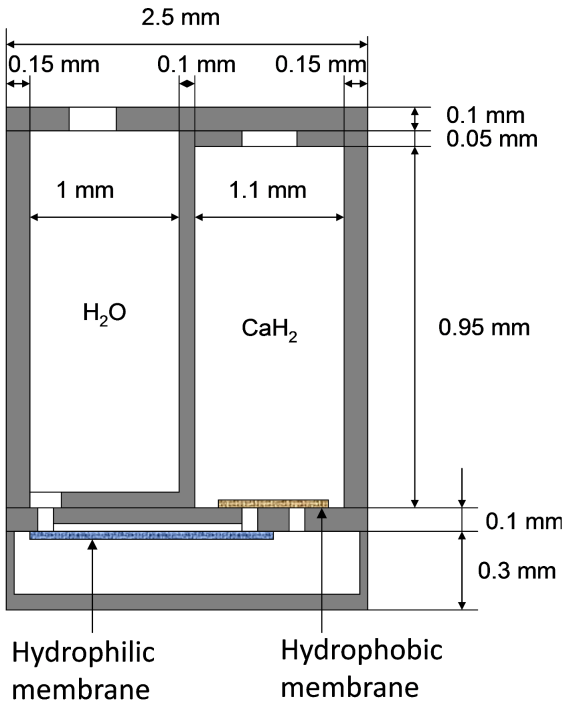

Figure 2.5: Schematic design of miniature CaH_2 hydrogen generator

green One 0.8 mm hole underneath hydride chamber covered with hydrophobic membrane on hydride side, with water chamber sealed.

purple Two 0.3 mm holes underneath hydride chamber. One of them covered with hydrophobic membrane on hydride side, with only one other covered with hydrophilic membrane on the MEA side.

From the experimental results, we observe that the hydrolysis reaction can be performed across different rates to deliver similar quantities of hydrogen. In the case when liquid water was directly supplied, or the water delivery hole was as large as 0.8 mm, the reaction rate was too fast for operating the fuel cell in low power regimes. In other cases, with water vapor being delivered in controlled quantities, hydrogen production followed a linear trend until stress failure from volume expansion. We believe that uniformity in hydrogen delivery is aided by the ability of water vapor to diffuse through the porous byproduct at lower reaction rates. In all five cases, we were able to produce sufficient hydrogen to meet energy demand $\geq$200 Whr/L. In three of the cases, when the control layer failed as indicated, liquid water flooded the reactor to produce hydrogen at very fast rates. This implies that the net available volume of the reactor for fuel loading is significantly reduced in order to prevent stress build-up and failure of either the chamber or the control layer.

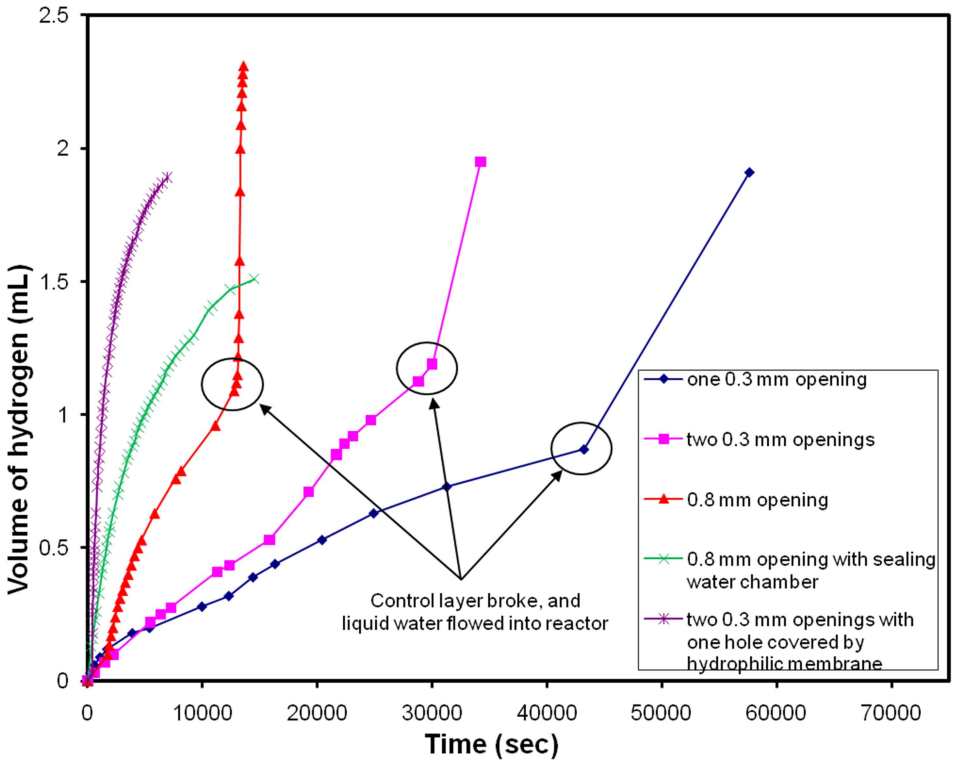

Figure 2.6: Experimental hydrogen production data from CaH_2 reactor

Following these observations, the reactor has been modified to be fabricated out of SS instead of Si, and the thickness of the silicon substrate in the control layer was increased to 300 μm. By controlling the ports and hydrophobicity at the reactor side, we are able to determine the limiting rates at which the MEA can function and produce current. When the demand is less than these limiting rates, the partial pressure of hydrogen is expected to build-up due to accumulation. On one hand, this is advantageous to the operating efficiency of the cell since we can maintain *greater-than-stoic* hydrogen pressure for improved reaction, however we are also limited by crossover and burst pressures of the PEM. Hence regulation is required, such that it can deliver within the range of these limiting rates and also suspend water supply to the reactor when the hydrogen demand subsides.

Chapter 3

Microfluidic control for self-regulated hydrogen supply

Having established a micro reactor for hydrogen supply to the MEA, with appropriate fuel loading and regimes of operation, it is necessary to miniaturize a control system that regulates the working of our device. A microfluidic approach has been adopted, combining a gas/liquid diaphragm microvalve and a surface tension driven channel pump. The microvalve is pressurized by hydrogen accumulated around the anode, to control the fluidic connection between the water reservoir and the reactor. A microchannel of shallow geometry, with appropriate surface treatment to render the walls hydrophilic, delivers water to the reactor due to surface tension. The design of this microfluidic control layer is such, meniscus pumping pressure is an order of magnitude greater than the operating pressure of the microvalve, that hydrogen backpressure acts on the valve before it can affect the working of the surface tension pump. In this chapter, we discuss the theory behind designing this microfluidic control layer and present results from protoype integrated devices (based on both CaH_2 and $LiAlH_4$) that have been fabricated[3].

3.1 Membrane deflection theory: linear elastic model

A thin circular membrane (t $\ll$ a) when subjected to uniform pressure, behaves similar to a uniformly loaded plate of finite thickness [38], [39], and its normal deflection thus assumes a parabolic variation in the radial direction as shown in figure 3.1. This deflection, within small strain limits, can be modeled by linear elasticity as follows. Consider an infinitesimally small ring element, of radius r and width dr. The deflection of this element is axissymmetric and is given by

$$w(r) = w_o \left(1 - \frac{r^2}{a^2}\right)^2 \tag{3.1}$$

Differentiating with respect to radius, the differential deflection at the element can be determined from

$$\frac{dw}{dr} = -\frac{4rw_o}{a^2}\left(1 - \frac{r^2}{a^2}\right) \tag{3.2}$$

[3]Some results using CaH_2 were published in [37], ©2009 IEEE, reproduced with permission from IEEE

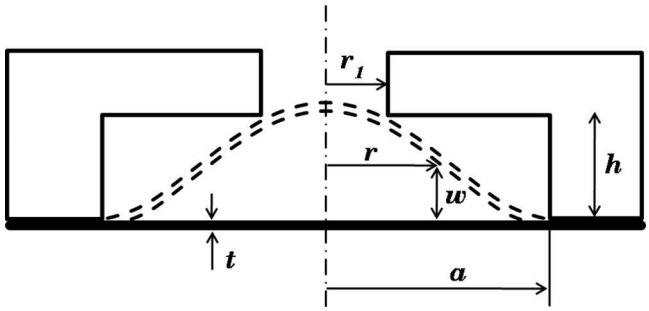

(a) Membrane before (solid) and after (dashed) deflection

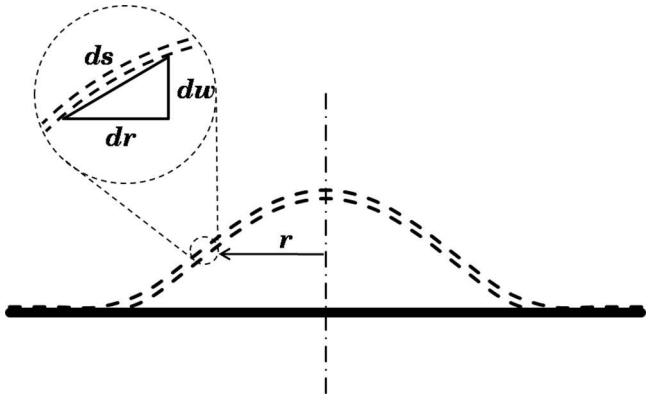

(b) Elemental shape change upon deflection

Figure 3.1: Schematic of polyimide valve in operation

The shape of the differential element can be approximated to the first order by triangulation as shown in figure 3.1(b), and its length estimated from pythagoras theorem

$$ds = \sqrt{1 + \left(\frac{dw}{dr}\right)^2}\, dr \tag{3.3}$$

As $\frac{dw}{dr} \ll 1$, this may be further simplified using binomial expansion as follows

$$ds \approx \left[1 + \frac{1}{2}\left(\frac{dw}{dr}\right)^2\right] dr \tag{3.4}$$

3.1.1 Maximum localized strain

The differential strain over the ring element is given by

$$\epsilon_r = \frac{ds - dr}{dr} \approx \frac{1}{2}\left(\frac{dw}{dr}\right)^2 \tag{3.5}$$

Substituting from (equation (3.2)), we have

$$\epsilon_r = \frac{8r^2}{a^4}\left(1 - \frac{r^2}{a^2}\right)^2 w_o^2 \tag{3.6}$$

Maximizing this strain by differentiating twice, and subject to the conditions $\frac{d\epsilon_r}{dr} = 0$ and $\frac{d^2\epsilon_r}{dr^2} < 0$, yields the root $r = \frac{a}{\sqrt{3}}$ as the location of maximum local strain. Corresponding to this location, the value of the maximum strain is

$$\epsilon_{r,max} = \frac{32}{27}\left(\frac{w_o^2}{a^2}\right) = 0.0475\% \tag{3.7}$$

3.1.2 Mean strain

The mean membrane strain is obtained by integrating deformation and averaging it over the radius

$$\epsilon_a = \frac{\int_0^S ds \, - \, a}{a} \tag{3.8a}$$

$$= \frac{w_o^2}{a}\int_0^a \frac{8r^2}{a^4}\left(1 - \frac{r^2}{a^2}\right)^2 dr \tag{3.8b}$$

$$\epsilon_a = \frac{64 w_o^2}{105 a^2} = 0.0256\% \tag{3.8c}$$

For a membrane of diameter 1000 μm, and 10 μm center deflection, both the maximum and mean strain are within limits of linear elasticity and therefore validate the plate theory model. Based on Timoshenko

and Woinowsky-Kreigers' solution [38] to this plate theory model, the pressure v/s deflection relationship for the membrane valve (including an empirical correction [40]) is given by

$$\Delta P = \frac{8}{3}\frac{Et}{a^4(1-\nu^2)}w_{max}^3 + \frac{4\sigma_o t}{a^2}w_{max} \tag{3.9}$$

For a polyimide (PI) membrane valve, with measured thickness of 2.3 μm, the valve closing pressure is estimated as $\Delta P = 3.68\,kPa$.

3.1.3 Valve actuation experiment

An experiment was performed to verify the theoretical model and validate the design of the passive membrane control valve. Test Specimens of above dimensions were microfabricated and examined using a back-pressure setup. The fabrication of these valves is discussed subsequently in section 3.4.1. The valves comprised of a 2 μm PI membrane, bonded to a 10 mm x 10 mm silicon die, with ports and channels for applying pressure. A pressure regulator, supplied with dry air from a tank, was used in combination with high-precision needle valves in order to pressurize the membrane. The exact pressure applied on the valve via the regulator was controlled through the voltage recorded by a pressure transducer (Omega PX142 differential pressure gage). Membrane deflection was imaged in an inverted optical microscope for different values of applied pressure.

Figure 3.2 shows results of this valve actuation experiment. The pictures have been enhanced with additional contrast for better visual clarity. The specimen has been tested and imaged at 3.10 KPa (0.45 psi), 3.45 KPa (0.5 psi), 3.79 KPa (0.55 psi), 4.14 KPa (0.6 psi), 5.51 KPa (0.8 psi) and 6.89 KPa (1.0 psi), respectively. When the valve is pressurized (applied from top, into the plane of the image), the membrane deflects towards the bottom wall. As the pressure is incresed in steps (3.10-3.45 KPa), the gap between the membrane and the wall decreases, until contact when a circular ring of fringing is observed to form in the image. This initiates at about 3.79 KPa. At this point, the membrane is deflection is sufficient to cover the water inlet port and close the valve. Further increase in pressure causes growth of the ring radius (4.14-6.89 KPa) as the valve closes further by the membrane getting pressed firmly against the bottom wall in a *zipping action*. Due to the compliance of the membrane, it assumes the shape of the valve die recess at very high pressure. The measured pressure on the membrane at which a visible fringe begins to develop due to valve closure, at 3.79 KPa, is commensurate with the model and differs from prediction by less than 3%.

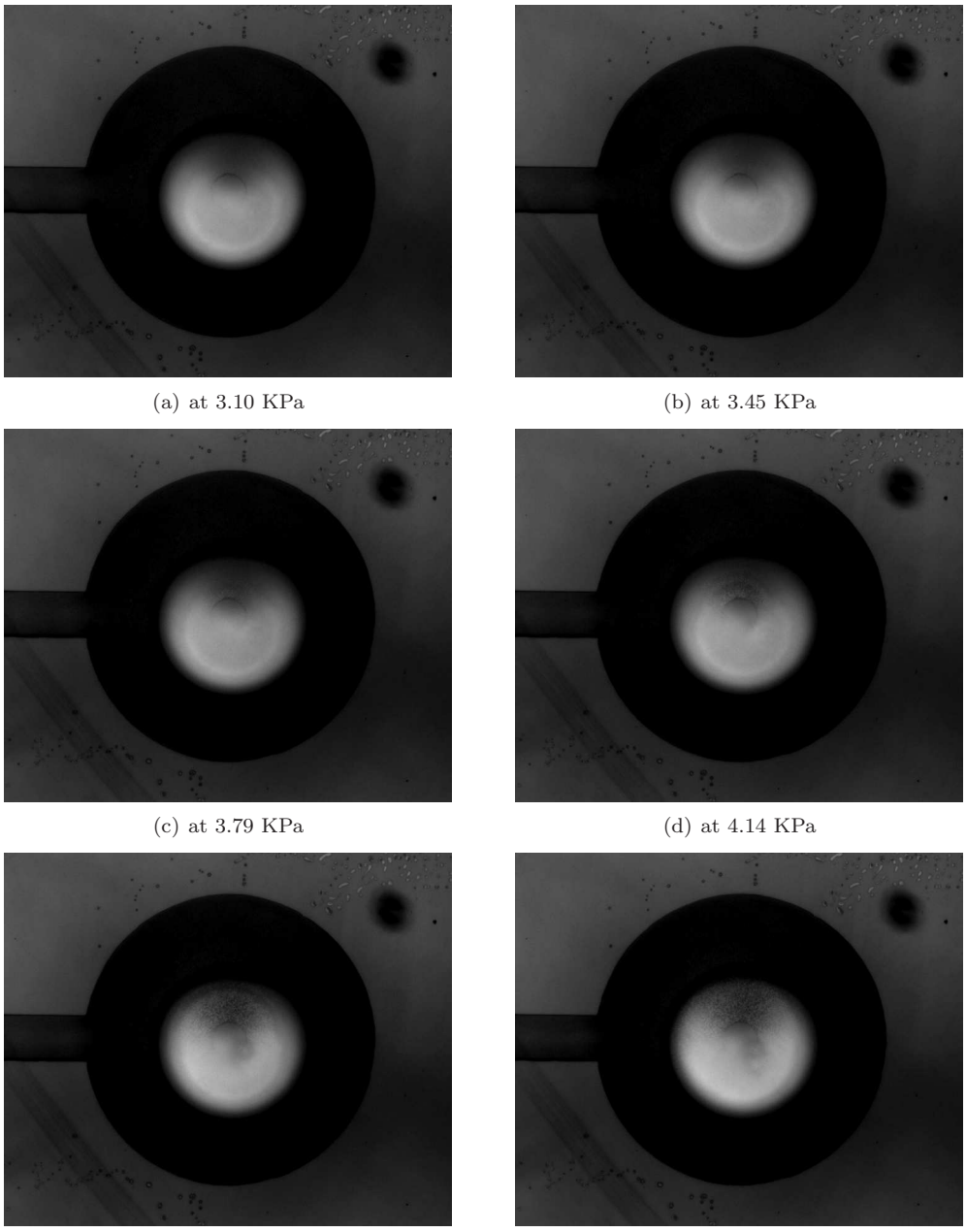

(a) at 3.10 KPa

(b) at 3.45 KPa

(c) at 3.79 KPa

(d) at 4.14 KPa

(e) at 5.51 KPa

(f) at 6.89 KPa

Figure 3.2: Micrographs of MEMS PI valve closing under back pressure

3.2 Surface tension pumping in a microchannel

3.2.1 Surface energy minimization

Surface tension is a force that scales down favorably, and attains significance over body forces, at micron dimensions. Ubiqitous in biological species and most notably for upward water transport in plants, it has

been demonstrated as a passive pumping agent in microfluidic systems. Walker and Beebe [41] have shown passive pumping of sub-μL volumes in PDMS channels, using surface tension effects. We adopt the concept in order to transport water from the reservoir to the reactor by means of a hydrophilic channel of suitable geometry in the control layer. Since the work of pumping arises from a surface force, it makes the micro fuel cell orientation independent.

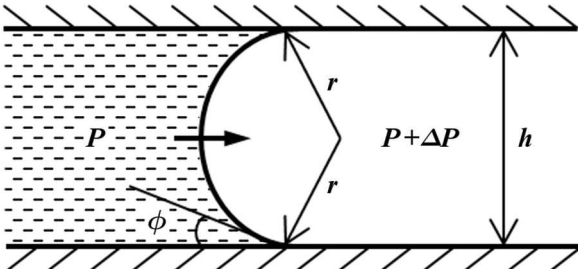

Figure 3.3: Surface tension pumping in a microchannel

Consider a rectangular microchannel, with hydrophilic walls, as shown in figure 3.3. Water is naturally drawn into the channel and the meniscus formed assumes a concave shape, whose radii of curvature r_1 and r_2 are determined by the channnel geometry and contact angle ϕ. Assuming that the meniscus is frozen in the channel under equilibrium, we have

$$2r_1 cos\phi = h \qquad 2r_2 cos\phi = w \tag{3.10}$$

The surface energy of an infinitesimally small arbitrary surface element on the meniscus is given by

$$dU = \sigma dA \tag{3.11}$$

where the elemental area as shown in figure 3.4 is defined by

$$dA = ds_1 ds_2 \qquad ds_1 = r_1 d\theta_1 \qquad ds_2 = r_2 d\theta_2 \tag{3.12}$$

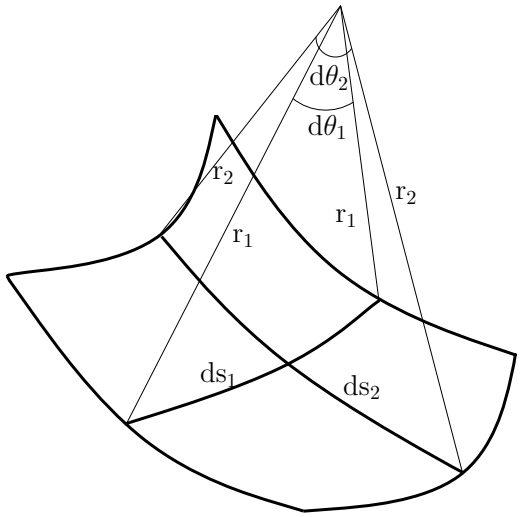

Figure 3.4: Curvature of an elemantal area of water meniscus

Integrating, the total surface energy of the meniscus is determined as

$$U = \int_A \sigma \, dA \tag{3.13a}$$

$$= \int_0^{\pi-2\phi} \int_0^{\pi-2\phi} \sigma \frac{h}{2cos\phi} \, \frac{w}{2cos\phi} \, d\theta_1 \, d\theta_2 \tag{3.13b}$$

$$U_\sigma = \sigma \frac{wh}{4cos^2\phi} \, (\pi - 2\phi)^2 \tag{3.13c}$$

If the channel width is set to parametrically vary with channel length, then

$$U_\sigma = \sigma \frac{(\pi - 2\phi)^2}{4cos^2\phi} \, h \, w(x) \tag{3.14}$$

Under this condition, the pumping force can be estimated as

$$F_x = \frac{\partial U_\sigma}{\partial x} \quad = \frac{\partial U_\sigma}{\partial w} \frac{\partial w}{\partial x} \tag{3.15}$$

$$F_x = \sigma \frac{(\pi - 2\phi)^2}{4cos^2\phi} \, h \, w'(x) \tag{3.16}$$

Hence for a hydrophilic channel of progressively decreasing geometry $w'(x) < 0$, surface tension acts to pump water and maintain the channel in an always filled condition, such that the surface energy of the meniscus is minimized. This phenomenon has been adopted to supply water from the reservoir to the hydride reactor for the hydrolysis reaction.

3.2.2 Pumping pressure: the Young-Laplace equation

The excess pressure due to surface tension, of a concave meniscus formed inside a hydrophilic channel (figure 3.3), is modeled using the Young-Laplace equation under equilibrium as follows:

$$\Delta P = \sigma \nabla \cdot \hat{n} \tag{3.17a}$$

$$= 2\sigma\kappa \tag{3.17b}$$

$$= \sigma \left(\frac{1}{r_1} + \frac{1}{r_2} \right) \tag{3.17c}$$

For a channel of width 150 μm, etched to a depth of 6.3 μm, and water-solid contact angle of ca. 5°, the excess pumping pressure due to surface tension is 24 kPa. In comparison, this is much greater than the pressure required to close the valve as shown in equation (3.9). Hence, when there is build-up of unconsumed hydrogen with drop in load on MEA, the valve closes well before excess hydrogen accumulation can move the meniscus. This immediately shuts off water supply to the hydrolysis reaction and sends the device into a suspended state—preventing the prossibility of pressure balancing of the valve from opening it up, which could flood the reactor with more water and create excess unwanted hydrogen resulting in control failure. On the other hand, during periods of high load, all the hydrogen gets consumed by the MEA and the resulting low/vacuum pressure on the membrane keeps the valve open with surface tension continuously pumping water for hydrogen generation.

3.3 The integrated micro fuel cell power generator

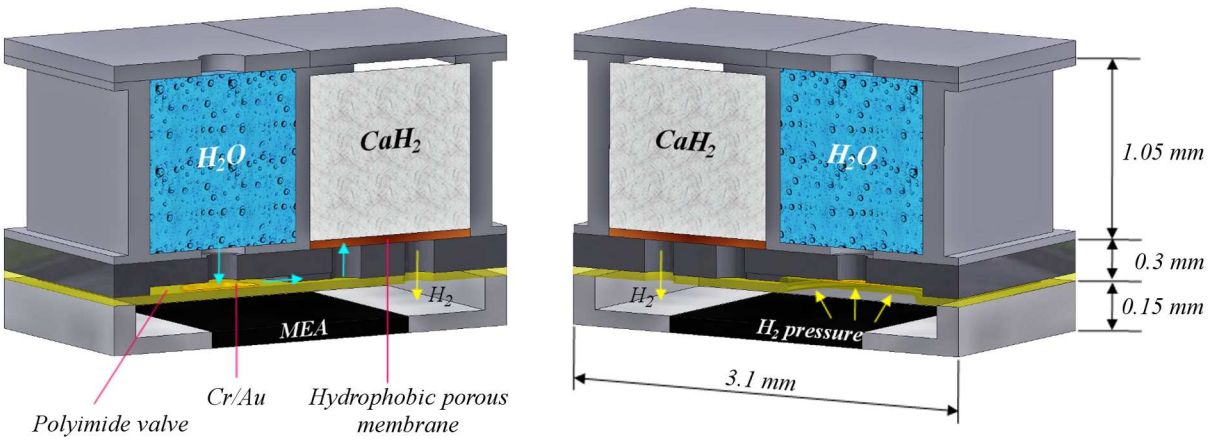

Figure 3.5: Schematic of the micro fuel cell power generator

A schematic of the integrated micro fuel cell, depicting the passive microfluidic pump and valve control scheme in operation, is shown in figure 3.5. The device consists of three distinct assemblies: a fuel store-cum-hydride reactor, a passive MEMS control layer, and the fuel cell MEA. As discussed in section 2.3.3, hydride fuel ($CaH_2/LiAlH_4$) and water reactants are packed in side-by-side chambers. The hydride chamber, loaded partially with due allowance for byproduct volume expansion, also serves as the reactor to release hydrogen gas when water is delivered from the reservoir by the MEMS control layer. The microfabricated control layer, as described above, comprises of a silicon surface tension pumping channel connecting the two chambers to supply water for hydrolysis and a polyimide membrane valve that regulates this water supply through feedback from backpressure of accumulated hydrogen. The assembly is such, an impermeable Cr/Au spot aligns with the water chamber port along with two other via ports for water delivery and hydrogen release facing the hydride reactors. The port configuration and choice of hydrophobic membrane at the reactor bottom have been derived from experiments in section 2.3.3. Hydrogen generated by this scheme is utilized at the anode of the MEA at a rate determined by electrical load. A spacer present between the MEA and the valve side of the control layer adds sufficient dead volume to provide a reserve of hydrogen for switching loads. The advantage of designing the valve out of PI membrane is that it's ability to absorb upto 4% water by weight ensures humidity around the MEA, preventing conductivity loss from dryout of nafion pores due to dessication by the hydride. The sizing of the device is such that it has a footprint of 0.96 mm^2 and volume of ca. 12.7 μL. The hydrogen generator occupies ca. 67% by volume of the device, and the control layer and MEA-spacer assemblies are as thin as 300 μm and 150 μm respectively. Figure 3.6 depicts a size comparison image of the completely integrated device, sealed with fuel, prior to water injection and operation.

3.4 Integrated device fabrication

The hydrogen generator (reactor), with rectangular water and hydride pockets, was electrical discharge machined (EDM) out of stainless steel (SS). A 200-400 μm sized hole was provided at the bottom of the water chamber, whereas the hydride chamber bottom was left open with an additional flange on the top to increase bonding surface. SS machining was preferred over Si microfabrication, based on failure of Si devices in previous experiments due to stresses arising from chemical swelling inside the hydride reactor. Material usage was thus economized and wall thickness reduced to 100 μm to improve volumetric energy density by increased fuel loading.

MEA preparation has been discussed in section 2.2.1 and figure 2.1.

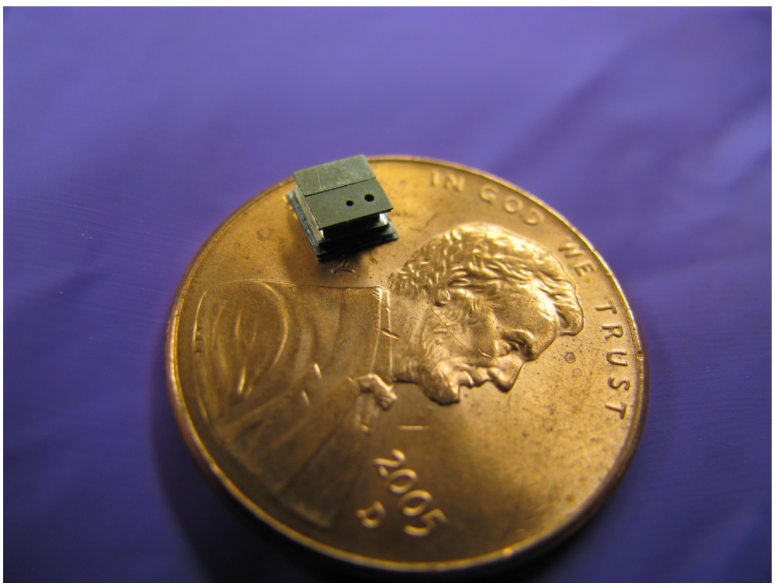

Figure 3.6: Photograph of the fully integrated micro fuel cell, in comparison with a U.S. 1 cent coin

3.4.1 Fabrication of the valve

Figure 3.7 shows a flow sheet for the fabrication process of the MEMS control layer. The microfluidic valve-chamber-cum-channels and via ports were patterned on a 300 μm Si wafer by conventional double-sided lithography in steps (a)-(d). The silicon die comprised of three holes– one (100/200 μm) connecting the water chamber to the valve inlet, another at the exit of the microchannel delivering water vapor to the hydride reactor, and a third for the exit of produced hydrogen to the MEA at the gas side of the PI membrane. A total of four different hole sizes were fabricated and tested on the hydride chamber side. The water vapor delivery hole was varied as 300/400/500 μm with the hydrogen exit hole being 300 μm, and in another case the two holes were a single connected slot with PI partially etched away for the hydrogen exit. The via holes and shallow channel featues (5 μm nominal depth) were dry etched by an SF_6/C_4F_8 plasma in a Plasmatherm^{TM} ICP-DRIE system to a measured depth of 6.3 μm. Following this, the Si dies were treated with SC-1 procedure (NH_4OH:H_2O_2:H_2O of 1:10:100 at 73°C) for 30 min in order to make the surfaces of the channel walls extremely hydrophilic ($\phi \leq 5°$) [42].

The PI membrane was prepared through a spin-cure-release procedure as outlined in steps (e) and (f). A 25 mm square coverglass handle substrate was treated with buffered HF oxide etchant to rough the surface for membrane release, and cleaned by the SC-1 procedure. HD Microsystems^{TM} PI 2545 precursor was spun at 3000 rpm (for nominal 2 μm thickness) and baked on a hotplate at 90°C for 30 min. Imidization to 2.3 μm final measured thickness was achieved, by vacuum annealing in a nitrogen atmosphere at 350°C

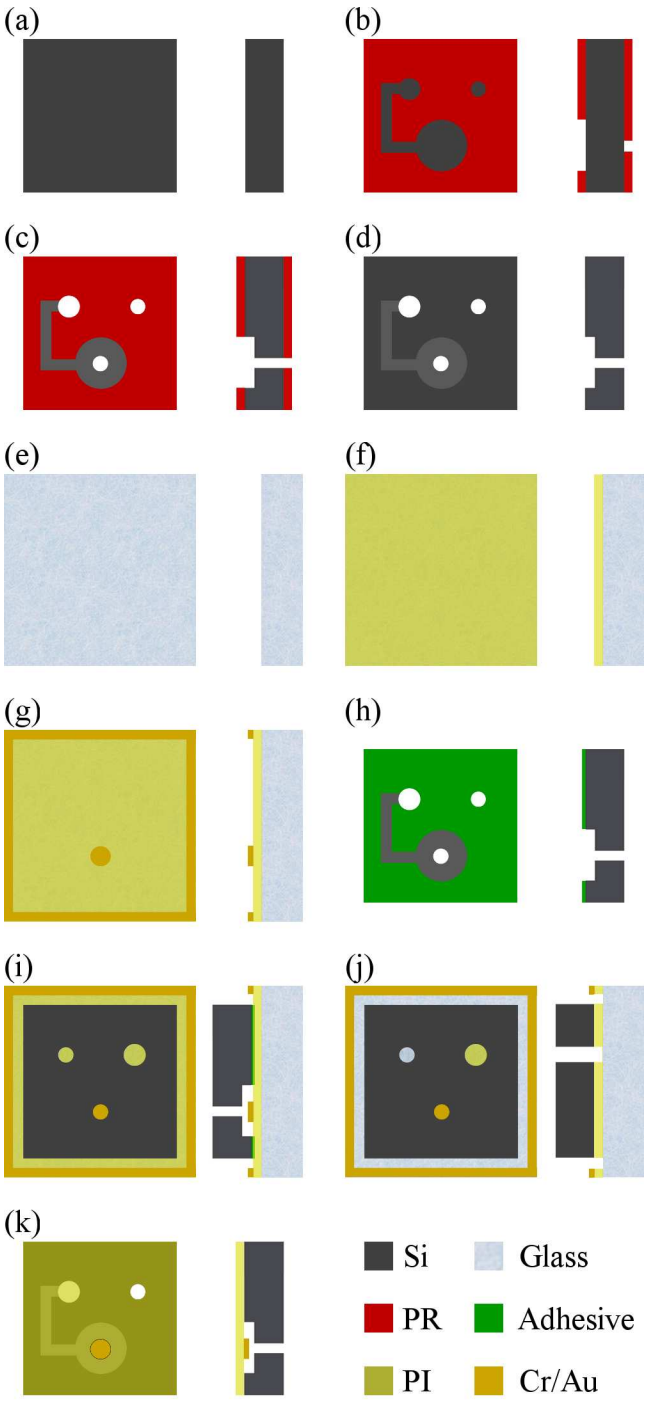

Figure 3.7: Fabrication sequence of the MEMS polyimide valve

for 3 hours. A 200 nm thick Au film (step (g)) on 5 nm Cr adhesion layer was sputtered onto the PI surface. Micromachined Si shadow masks, with patterns of alignment marks and the 200/300 μm Cr/Au spot for covering the 100/200 μm water hole, were used for this process. Bonding between PI and Si was

accomplished by an in-house adhesive transfer process [13]. A thermal epoxy resin was transferred onto the Si die by PDMS contact lithography (step (h)). Using Si shadow mask, adhesive covering the channel and valve regions was etched away in a Jupiter^{TM} Oxygen Plasma RIE. After pattterning of the adhesive, the Si die and PI membrane were brought in contact, with alignment of the Cr/Au covering the water chamber port under a microscope, and thermally bonded on a hotplate at 140°C under pressure (step (i)). PI outside of the Si die, and the region covering the hydrogen exit port was etched using the Oxygen Plasma, with shadow masks (step (j)). Bonded PI membranes were finally released from the coverglass substrate by swelling in a DI water bath on a 120°C hotplate in an overnight soak. The released control valve dies (ca. 3 μL) were cleaned and dried, for eventual integration (step (k)). Figure 3.8 shows pictures of the microfabricated control layers.

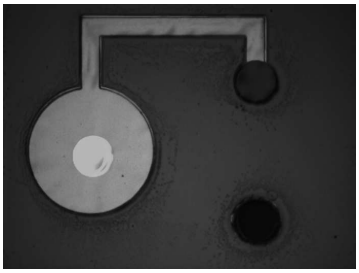

(a) Control layer showing valve, channel and ports

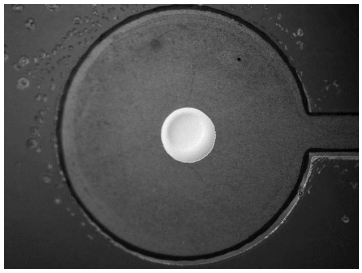

(b) PI circular membrane valve with Cr/Au covering water port

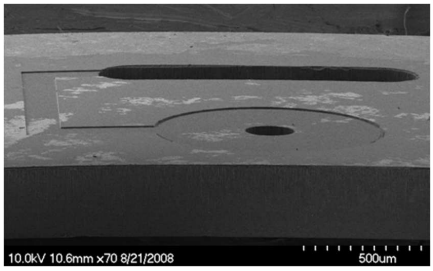

(c) Scanning electron micrograph of a Si control layer with a slot opening at the reactor

Figure 3.8: Microscopic images of the control layer

During integration, a 25 μm thick PTFE hydrophobic membrane was attached to cover the ports on the hydride side of the valve. The three layers—hydride reactor, control layer and MEA—were stacked, along with a 50 μm SS spacer between the control layer and MEA, and bonded using two-part epoxy resin as shown in figure 3.9. Finally, the device was loaded with powdered CaH_2 or $LiAlH_4$ (Aldrich Chemical Co., St. Louis, MO) and capped with a SS cover using Loctite Super Glue^{TM}, in a Nitrogen Glovebox.

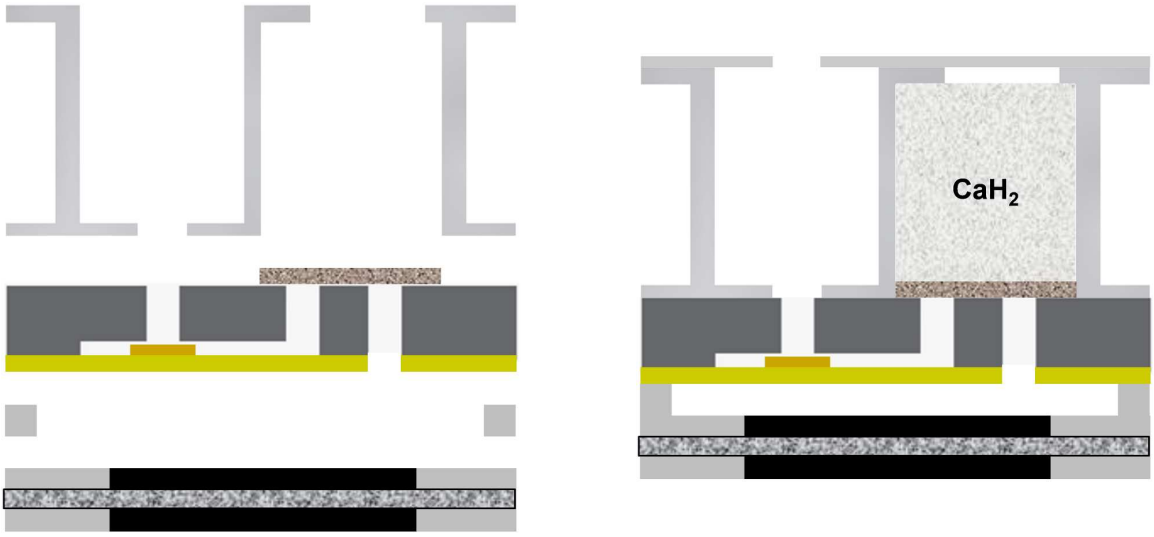

(a) Stacking of device layers during assembly

(b) Integrated device loaded with CaH_2 and sealed

Figure 3.9: Schematic of integrating the H_2 generator, MEMS control layer and MEA

3.5 Experimental Results

Prototype integrated devices, loaded with both CaH_2 and $LiAlH_4$ fuels, were tested using a Solartron 1287^{TM} Potentiostat. Polarization curves were generated by continuous ramping of cell potential between open circuit and short circuit conditions and the available current was measured. While performing lifetime tests and switching, the potentiostatic mode was chosen and chronoamperograms were drawn. Throughout the tests, the cathode was run at ambient humidity and quiescent air. Experiments on the MEA, prior to integration, were performed by supplying dry hydrogen from a tank to the anode using an appropriate package.

3.5.1 Polarization and power density

A comparison of polarization and corresponding power density plots of integrated devices for both CaH_2 and $LiAlH_4$ fuels, with an unintegrated MEA fed with H_2 gas from a tank, is shown in figure 3.10. The performance shows distinct effects arising out of integrating an MEA with an on-board hydrogen source of finite capacity and delivery. Since the fuel cells are exposed to ambient air at the cathode, the performance now depends directly on the availability of hydrogen and its catalysis at the anode. The polarization curve of the MEA itself (unintegrated) shows an activation region from open circuit down to 0.8 V, followed by ohmic behavior with peak power density occuring at ca. 0.4 V. We do not observe the mass transport limited regime within the MEA due to thin PEM construction (25 - 50 μm) of the miniaturized assembly, and the MEA seamlessly transitions from ohmic behavior to short curcuit. In contrast, regardless of the type of fuel

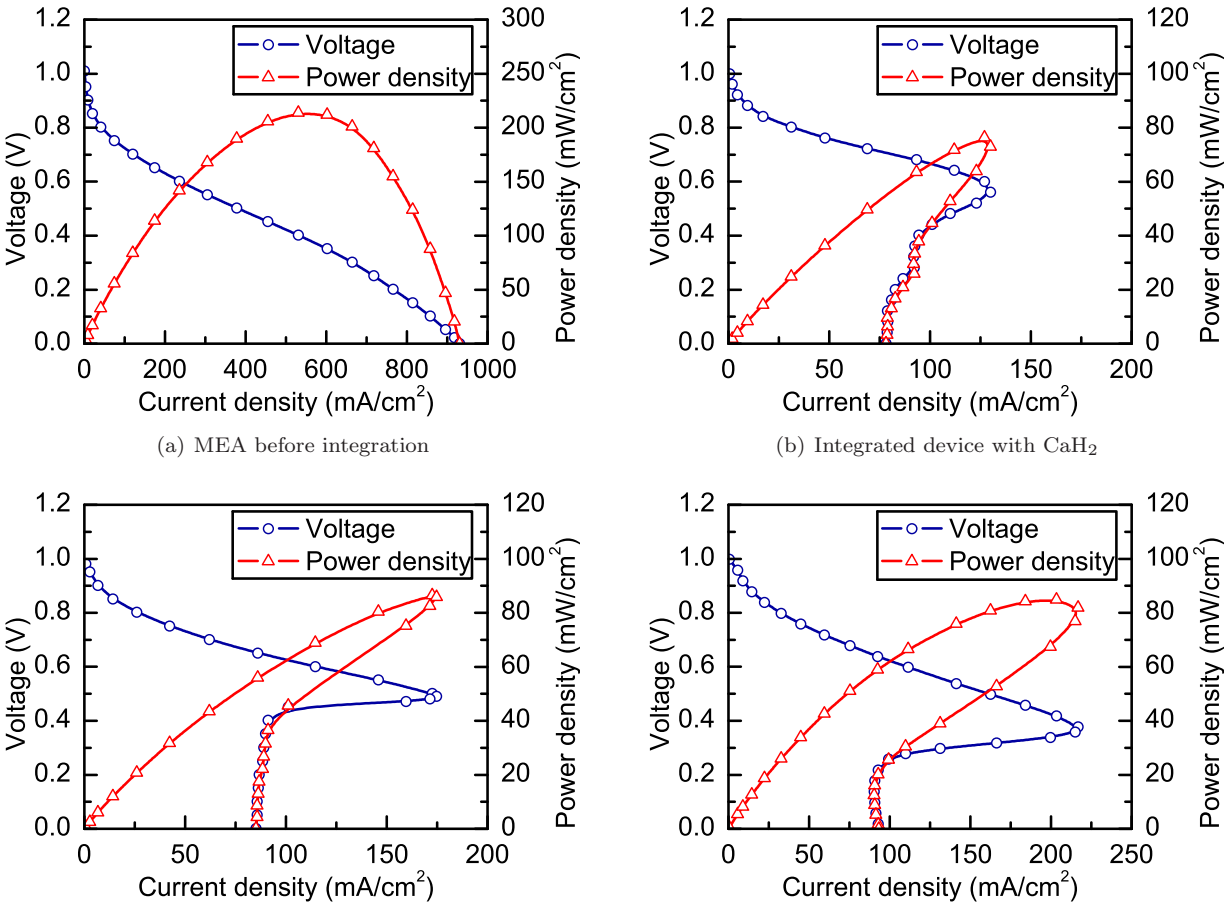

(a) MEA before integration

(b) Integrated device with CaH_2

(c) Integrated device #1 with $LiAlH_4$

(d) Integrated device #2 with $LiAlH_4$

Figure 3.10: Polarization and power density plots of integrated micro fuel cells

loading, all three integrated devices show diminished performance.

Firstly, the activation behavior extends down to 0.75 V, with ca. 50% drop in in current density. This may be attributed to the difference in partial pressure of hydrogen at the anode, between integrated devices and the packaged MEA. Whereas the hydrogen is fed from a tank directly through the package for the MEA and this enables sustanining higher-than-stoic ratios at all times, the hydrogen partial pressure in integrated devices is controlled by the closing pressure of the microvalve. Once hydrogen accumulates to the valve closing pressure, water pumping through the the microchannel is shut and this prevents further hydrogen production to higher pressure. As a consequence of this limitation, by design, we observe the drop in performance in the activation regime. We could argue based on the data that the valve be designed for higher pressures in order to accommodate better performance, but the valve design itself is limited by two other constraints: the surface tension pumping pressure that moves water meniscus in the microchannel is

required to be much higher than the valve closing pressure, and the tendency of hydrogen to profusely leak through materials at higher pressures could make long term performance very lossy.

Secondly, the ohmic region is much steeper with upto 80% decrease in comparison with the unintegrated MEA. In this regime, the MEA operates in such a way that hydrogen demand is a combination of both pressure and flow rate. While this can be satisfied by supplying hydrogen gas from a tank, the integrated device is accompanied by its limitations in the rate of hydrogen production. We explain this by identifying two separate timescales associated with the processes in the integrated device. One of them, the timescale of hydrogen catalysis and proton transport in the MEA, is a fast process. The other being the timescale associated with the rate of water pumping and diffusing through a porous packed bed to react and diffuse out hydrogen, is much slower. The latter phenomena particularly dominate the integrated device as the rate limiting agents, and the reactor is unable to deliver hydrogen at the partial pressure required by the MEA at these rates. Instead, the MEA shifts to a mass transport limited mode, operating less eficiently with lesser-than-stoic hydrogen pressures at the same flow rates. This regime extends to the point of peak power density of ca. 80 mW/cm^2, observed between 0.4 - 0.5 V.

Thirdly, all of the integrated devices are fully mass transport limited when operated below 0.4 V. In this region, the ion-transport rates are so high that any hydrogen molecule that comes in the vicinity of the anode is almost instantaneously oxidized and the protons are conducted through the PEM. The MEA is able to deliver high current density when flooded with hydrogen from the tank. However, the micro hydrogen generator is unable to meet the demand even when suplying hydrogen at its performance limit, with the valve fully open and microchannel continuously pumping water for hydrolysis. Hence, there is a sudden drop in performance signifying this limitation as the device operates further away form equilibrium. In this regime, the available power density decreases by a whole order of magnitude. Note the similarity of this fully mass transport limited regime to that of the typical fuel cell characteristic described earlier in figure 1.2, albeit the difference here being that the mass transport limitation is attributed to the dynamics of hydrogen generation and not ion transport.

As a consequence of being fully mass transport limited, the polarization curve undergoes sharp reversal in the current density. While the skewed shape of this curve appears anomalous because of multiple solutions to the voltage at the same current density (for example, in figure 3.10(d), the device may operate at either 0.6 V or 0.3 V at 100 mA/cm^2), we can understand this better by performing the polarization in both forward and reverse directions. Figure 3.11, shows the polarization curve for the same $LiAlH_4$ loaded device, but in this case the test was perfomed in a complete loop beginning from open circuit to short circuit and back to open circuit. In this case, the polarization curve follows a different path in the reverse direction.

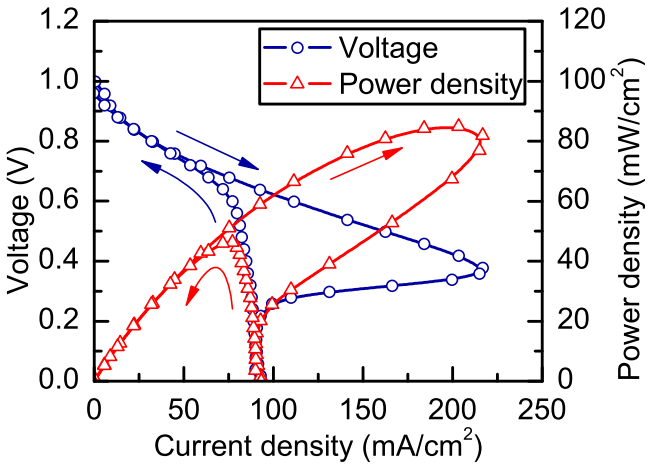

Figure 3.11: Polarization and power density loop plots for an integrated device loaded with $LiAlH_4$

At the same voltages, the power density developed in the reverse direction is much less than in the forward direction. We attribute this difference to the the dead-volume effect of the spacer around the MEA. When operating in the forward direction, the reactor is able to supply hydrogen at stoichimetric pressure and rates at higher voltages. This is advantageous for dropping the MEA voltage while switching to higher power regime—as the excess hydrogen in the dead volume is momentarily able to cater to the demand before, the device hits mass transport limits, it enables the ohmic region to extend further out to higher current density. Beginning in the reverse direction from short circuit, however, the hydrogen demand at the anode is so high that there is no accumulation. As we ramp up in voltage, the demand changes from flow rate to partial pressure and the reactor stuggles to build up hydrogen pressure, the MEA is forced to operate at low efficiency with under-stoic hydrogen. This effect is nullified as we approach the activation regime, since the hydrogen demand is sufficiently low that the reactor can quickly evolve hydrogen and make up the stoichimetric ratios.

When operating the micro fuel cell, it may not be possible to determine the V-I characteristic based on just one direction, for the response is path dependent—akin to a hysterisis effect. The presence of dead volume at the anode is advantageous for switching to short bursts of high power and, as a side effect, the device gradually recovers its operating efficiency while reverting back to the extended periods of low power density operation.

3.5.2 Lifetime performance tests

On the basis of polarization behavior observed upon integration, the prototypes were operated in multiple regimes with switching, to extract lifetime performance characteristics. We chose to run the devices for extended periods of low power demand close to the activation region (0.8 - 0.9 V), with switching down (0.3 - 0.4 V) intermittently to simulate peak power demand. The device was also operated in purely ohmic mode (0.6 V) to observe effects on uniformity of delivery.

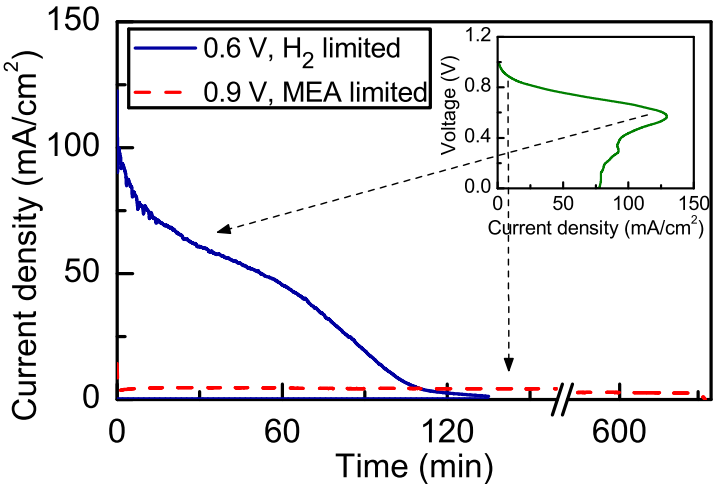

(a) Chronoamperograms at 0.9 V and 0.6 V (inset shows polarization curve from figure 3.10)

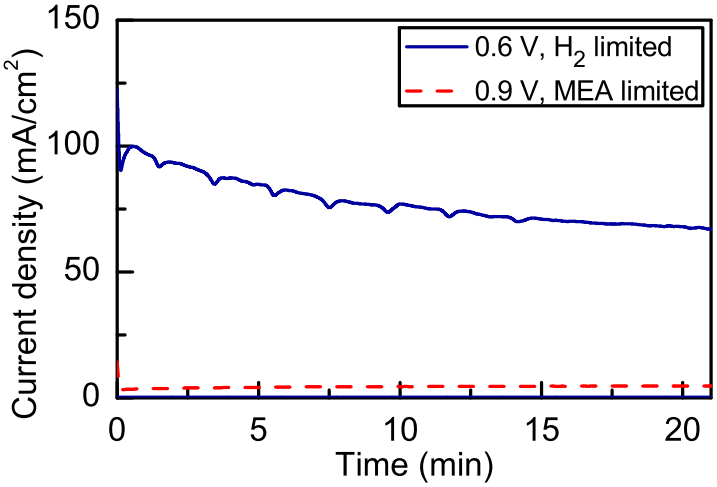

(b) Chronoamperogram at 0.9 and 0.6 V, zoomed-in from t=0 to 20 min

Figure 3.12: Lifetime performance of the integrated micro fuel cells in activation and ohmic regimes

A comparison of lifetime performance of the integrated micro fuel cell when operating at different voltage is shown in figure 3.12. Two separate devices loaded with CaH_2 fuel were operated entirely in the activation (0.9 V) and ohmic (0.6 V) regimes respectively, based on the inset polarization curve in figure 3.12(a). In

the former case, the current drawn from the MEA was low as it occured under low power demand of the activation regime. As a result, the hydrogen generator was expected to meet the stoichiometric requirement for hydrogen at the anode, with the MEA reaction rate being the limiting factor. Consistent with this mode, the micro fuel cell maintained a uniform current density of ca. 10 mA/cm^2 and operated for over 10 hours. The latter case where the power demand on the fuel cell was greater, closer to the peak power density, the device struggled to keep up uniformity in power delivery. In this mode, the reactor could not deliver hydrogen at the rate and partial pressure required at the anode thus making the device hydrogen limited. Further, the current density progressively decreased over time, indicative of mass transport effects. This correlates with diffusion limitation, over time along with volume expansion, of water vapor thorugh byproduct hydroxide/hydrate in the hydrogen generator before reacting with fresh CaH_2 to release hydrogen. In essence, the gradual drop in current density while operated in ohmic regime follows the increasing diffusion length for water vapor inside the reactor for effecting hydrolysis, once water has been pumped through the microchannel. In this intermediate regime, the device operated for 2 hours and could deliver 152 Whr/L.

Figure 3.12(b) shows the same chronoamperograms, but zoomed in for the first 20 minutes of the lifetime tests. During this period, we observe that the performance in the activation regime at 0.9 V built up to ca. 4 mA/cm^2 and remained uniform throughout for most of the testing period. In contrast, while we already showed that at 0.6 V ohmic region the current density gradually dropped, we can see the operation of the valve in this timeframe. We observe that, periodically, the current density curve dips momentarily and recovers quickly to settle again into the progressive decay mode. Each one of these points is representative of the valve opening, when the hydrogen pressure around the MEA drops significantly upon consumption, to let water through the microchannel. The valve closes again when the pressure builds up due to hydrogen that evolves from the hydrolysis reaction. While the gradual decay in current density over the entire lifetime test is related to water vapor diffusion limitation inside the reactor, the current density at those moments in time when the valve opens also decreases each time. That is, for the same local minimum in hydrogen partial pressure (this value is determined by the hydrogen backpressure at valve closing/opening) inside the device, the MEA performance appears to be degrading in time. In combination with water vapor transport, this acts as the limiting factor in determining how the device performs in the ohmic regime. Beyond 15 minutes of the test, we did not observe any local minima in current density. This suggests that the hydrogen partial pressure was always less than that required to keep the valve closed, so that it functioned in an always open mode to continuously supply water to the reactor. The device performance was only dependent on water vapor diffusion, and the fuel cell operated free of any regulation from the control layer.

We establish that operating the integrated micro fuel cell close to equilibrium is able to provide uniform

power delivery over extended periods, whereas the transition region where the fuel cell gets increasingly mass transport limited shows gradually decreasing current that is consistent with the mass transport effects in hydrolysis.

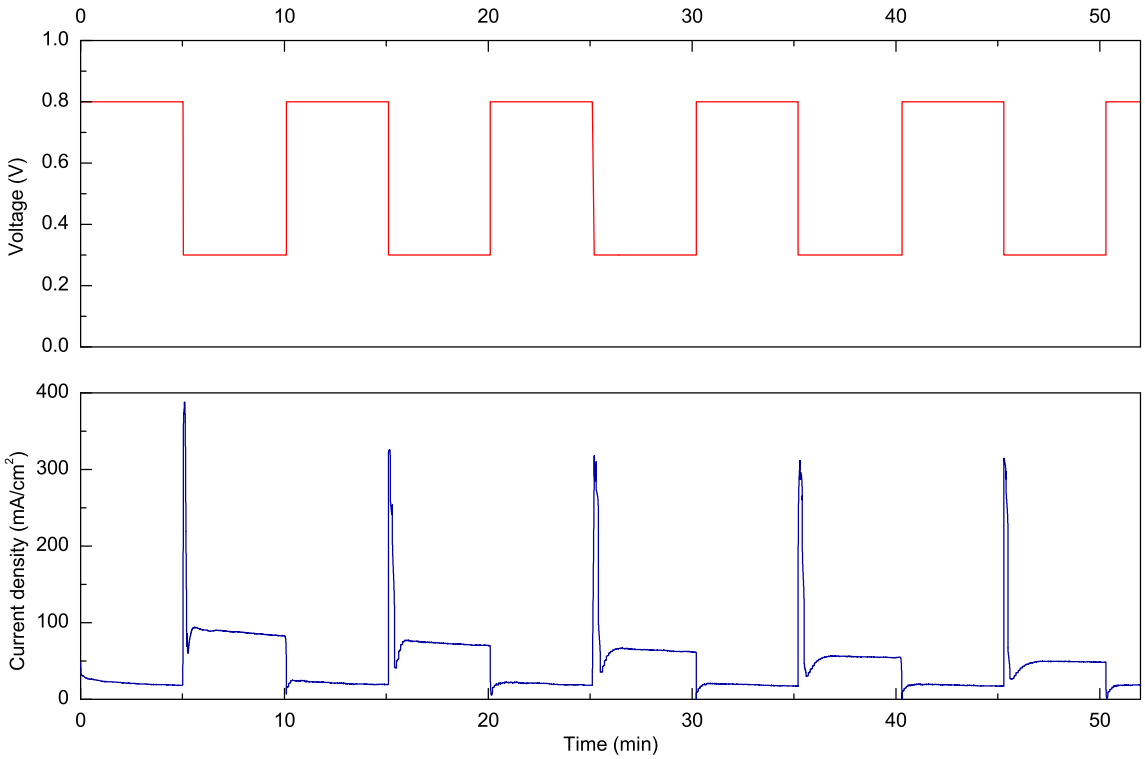

Figure 3.13: Switching action of integrated device loaded with CaH_2 between 0.8 and 0.3 V

Performance of the integrated micro fuel cell, under dynamically varying load, is depicted in figure 3.13. As shown in the voltage-time curve, the test was performed in such a manner that the operating voltage of the fuel cell followed a square wave, between 0.8 and 0.3 V with 10 min timeperiod. The bottom graph shows current density snapshot for five consecutive periods. During each cycle of switching, we can divide the response curve into three distinct regions. During bulk of dwell times at both 0.8 and 0.3 V, the fuel cell response was consistent with polarization tests, with the device activation limited at 0.8 V and fully mass transport limited at 0.3 V. At the time of switching to high electrical load, current density momentarily spiked up due to accumulated hydrogen at high partial pressure at the anode. While this spike lasted for ca. 10 s duration, the time it took for excess hydrogen around the anode to be consumed, it corresponded to the peak power density provided by the micro fuel cell. Following this, the hydrogen pressure dropped to levels at which the valve opened and closed so that water could be pumped in the microchannel for hydrolysis reaction to set in and cater to the high hydrogen demand at low voltage. At this instant the current density

sharply decreased, and then gradually rose towards the bulk dwell value at a rate that tracked the hydrogen generation. When the load dropped and the device switched back again from 0.3 V to low power demand at 0.8 V, the current density dropped instantly to zero because of low hydrogen partial pressure. At this point, the valve being open allowed more water to pump into the reactor and continued generating hydrogen. As the consumption rate at 0.8 V was lower, it allowed accumulation at the anode, enabling the partial pressure to build up. Once this rose to levels that matched the MEA's requirement and closed the valve, the device had completely switched back into the activation regime of operation as indicated by the recovery of current density to its bulk dwell value at 0.8 V. Note that although the current density took a few seconds to completely transition between the two load regimes, the device was able to instantly deliver peak power density of 369.19 W/L, and sustain this for upto 10 s.

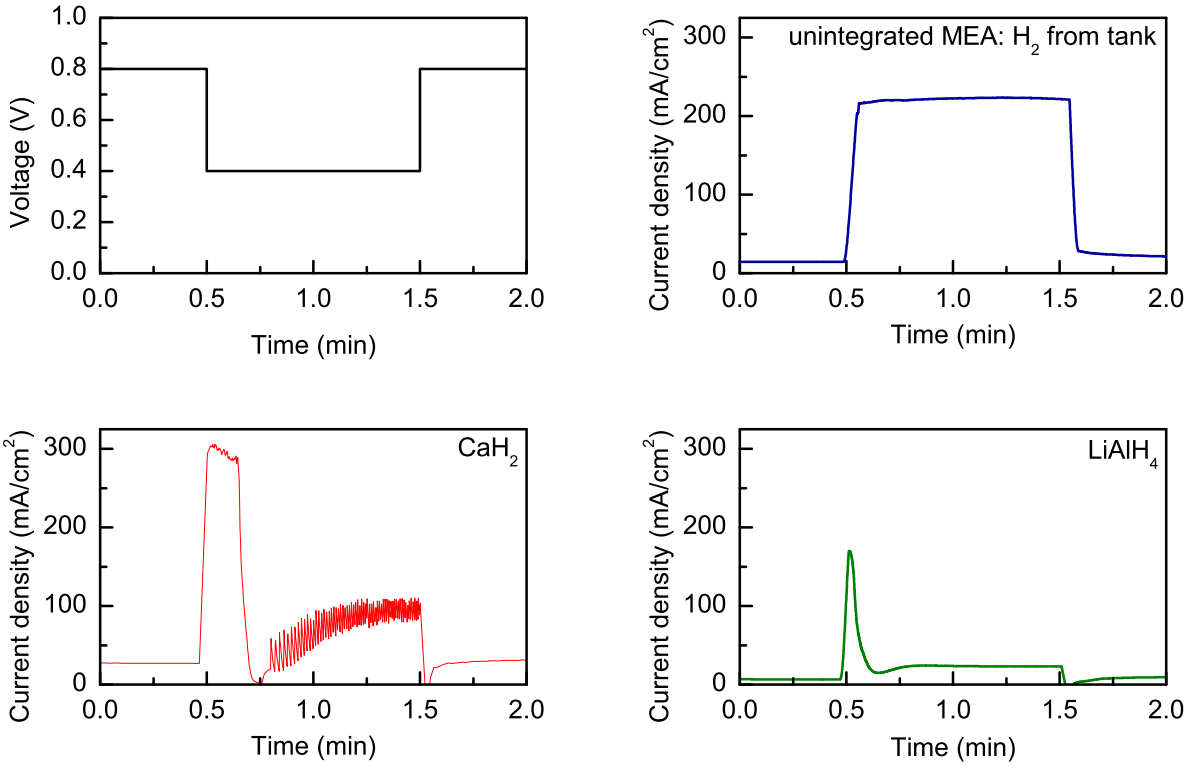

Figure 3.14: Switching behavior of integrated devices between 0.8 and 0.4 V for various fuel loadings

Figure 3.14 shows current density snapshots of switching of the micro fuel cell, for both CaH_2 and $LiAlH_4$ hydrogen sources, under identical test loads and duration. The test was performed between 0.8 V and 0.4 V, with 1 min dwell time at high power demand as indicated. An unintegrated MEA (after disintegration from the CaH_2 device) was also tested, with dry hydrogen supplied from a tank. In this test, we observed the switching action and its accompanying transition effects as described above, for both of the integrated

devices. On the whole, the performance of the $LiAlH_4$ loaded device was poorer than that with CaH_2, as seen from the current density during the bulk dwell times at both voltages. This corresponds directly to differences between the MEAs that these devices were integrated with. Further, the peak power spike that followed during switching was more pronounced in the case of CaH_2 than with $LiAlH_4$. Although it was partly attributed to differences between the respective MEAs, we also observed that the peak power region was narrower for the device with $LiAlH_4$. The width of the peak was related to the amount of accumulated hydrogen and its amplitude to the partial pressure. In the case of $LiAlH_4$, the result indicated that the device did not have as much excess hydrogen, as with CaH_2. We attribute this to intrinsic differences in the rate of hydrogen production between the two sources. That is, CaH_2 hydrolyses quicker than $LiAlH_4$ becasue of its larger volume expansion—the more porous the byproduct bed, the easier it is for water vapor to diffuse through.

In comparison with the integrated devices, the direct hydrogen fed MEA responded differently, in a square wave pattern. Operating with stoichiometric hydrogen throughout, the unintegrated MEA was able to settle almost instantly into either regime during switching. The kinetics of the cell reaction and proton transport through Nafion were both sufficiently quick that they were not the rate limiting factors for miniaturizing the fuel cell, as discussed in 3.5.1. We infer that the dynamic of hydrogen generation, particularly based on the mass transport effect associated with the porosity and volume expansion of byproduct bed, was the rate limiting factor and this solely determined the switching capability of the micro fuel cell. Note that the power densities, both at the bulk dwell times and the spike, for the CaH_2 loaded device was higher than the power density at 0.4 V for the unintegrated MEA. This was because, at large flow rate, hydrogen from the tank dried the MEA, affecting proton conductivity. Whereas with the integrated devices, by design, the anode side was always kept moist by the PI valve to maintain proton conductivity.

Integrated devices, with both CaH_2 and $LiAlH_4$ reactors, were tested for lifetime performance. The resulting chronoamperograms are plotted in figures 3.15 and 3.16. Both devices were operated at 0.8 V throughtout the tests, with three instances of switching to 0.4 V for simulating increased power demand. The device with CaH_2 was was switched at 15 minute intervals, whereas the $LiAlH_4$ device was switched every hour. Both devices were able to maintain current delivery for over 3 hours, indicative of the hydrogen generator to provide stoichiometric hydrogen. The difference between the devices was that the current density provided by the CaH_2 device was, initially for an hour, nearly double that of the $LiAlH_4$ device. This relates directly to differences in the performance of the respective MEAs. Also, the curve for the CaH_2 device was relatively flat in comparison with the $LiAlH_4$ device whose current density varied like a half sinusioidal wave. Such a variation corresponds to the timescale of the microvalve opening/closing to

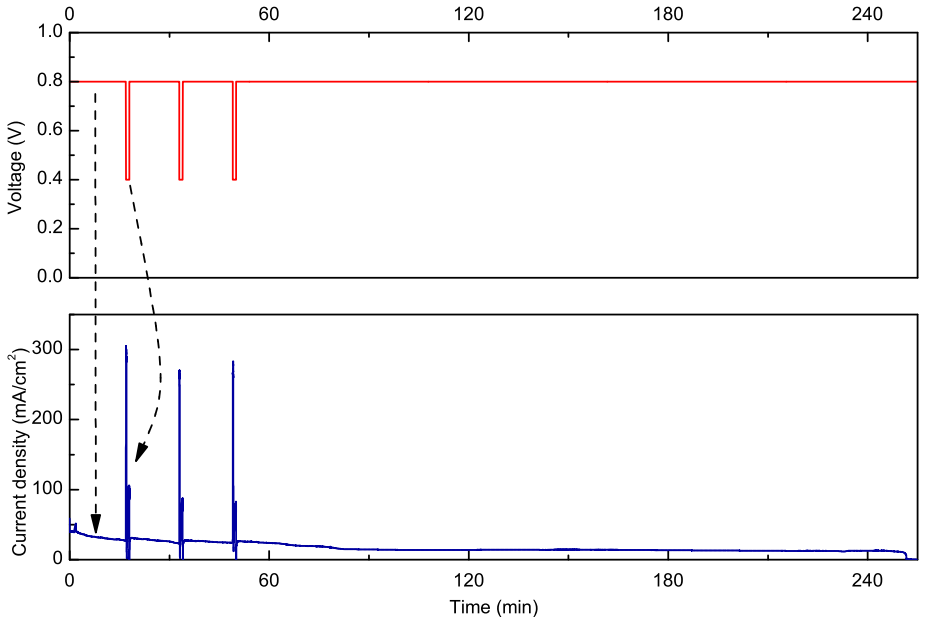

Figure 3.15: Chronoamperogram of integrated device loaded with CaH_2 with switching

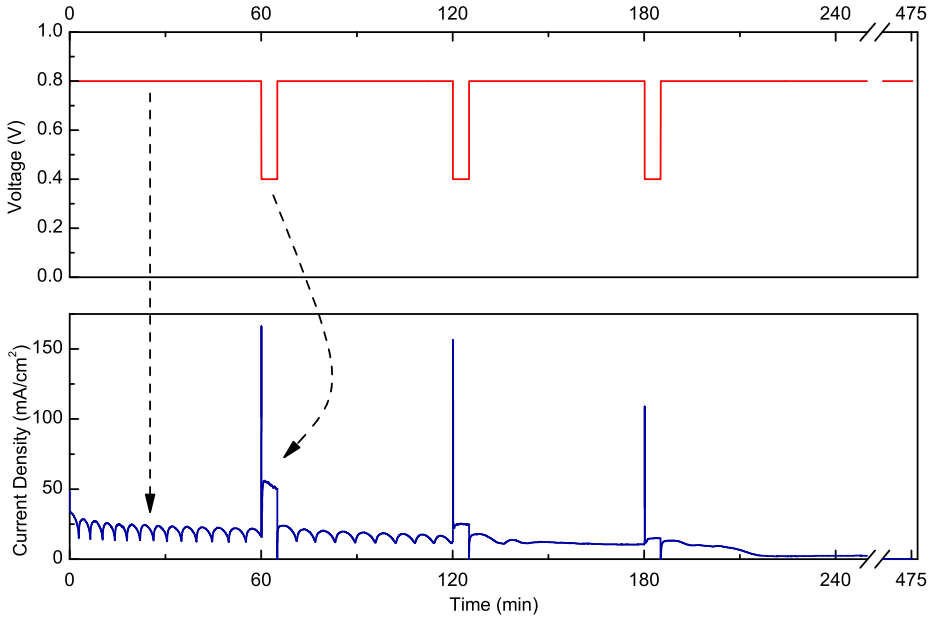

Figure 3.16: Chronoamperogram of integrated device loaded with $LiAlH_4$ with switching

pump water into the reactor, its vapor diffusion and consumption during hydrolysis. During switching, both devices demonstrated sharp power density peaks and evetually settled into the dwell period current density as discussed above. While switching back under low load, the devices recovered their current density at 0.8 V, just as before switching. Both devices supplied most of their energy densities within ca. 4 hours of

testing.

No.	Fuel	Cell Voltage (V)	Test duration (hr)	Energy Density (Whr/L)	Peak Power density (W/L)
1	CaH_2	0.8, 0.3	1.67	82.98	369.19
2		0.9	10.5	85.57	31.86
3		0.6	2	152.08	159.38
4		0.8, 0.4	4.25	148.32	302.85
5		0.8, 0.4	14.1	162.85	186.57
6	$LiAlH_4$	0.8, 0.4	48.5	161.96	151.33
7		0.8, 0.4	8	130.17	168.77
8		0.8, 0.4	26.25	195.97	215.26
9		0.8, 0.4	4.5	87.61	391.85

Table 3.1: Measured performance characteristics of integrated devices with microfluidic control

From lifetime performance of a number prototypes loaded with both CaH_2 and $LiAlH_4$ fuels, with tests spanning multiple regimes, switching and pulsed operation, the micro-integrated fuel cell system was able to deliver high energy density at both μW and mW power demand situations. Energy density and power density metrics for these devices are shown in table 3.1. In summary, the micro fuel cell could meet system milestones of nearly 200 Whr/L energy density and developed peak power density of upto 392 W/L, working in a completely self-sufficient mode with self-regulation that smartly tracked variations in electrical load on the order of seconds.

Chapter 4

The water recovery micro fuel cell: hydrolysis using byproduct water

4.1 How the micro fuel cell turned waterless?

In the previous chapter, we described a fully integrated prototype micro fuel cell that operates with passive microfluidic valve control and consistently delivers high energy with on-demand peak power density. During experiments with one such device, for microfluidic control of the fuel cell, a lifetime performance test failed. Upon disassembling the specimen to observe possible causes of failure, we concluded that faulty epoxy bonding of the control layer clogged the microchannel and rendered it incapable of transporting water to the microreactor. The device had worked though, with CaH_2 still getting hydrolysed, and delivered at very low power density. While it did not consume any of the on-board water, CaH_2 drew water vapor through the MEA (and hydrophobic PTFE membrane via the tiny H_2 delivery port in the control layer) from the ambient humidity. This mechanism was driven by the strong hygroscopic behavior of the hydride.

Could this mean that the micro fuel cell be further simplified? The capacity of such a system is still limited by the packaging of a control system on-board, and sharing approximately half of the on-board fuel storage volume with stoichiometric water. That means the energy density contributed to in such a system would be limited to ca. 25% of system volume, as shown in figure 2.5. In an alternate approach to maximizing the energy density of the 10 μL micro fuel cell, we eliminate the microfluidic control layer and on-board water to increase the volume fraction of the fuel. The operating principle of such a water recovery micro fuel cell (WRMFC) is based on water recovery at the cathode, and this chapter presents the design and fabrication of this device along with performance characteristics[4].

4.2 Recovering product water from cathode for fuel hydrolysis

Metal hydrides are known to be strongly hygroscopic. A natural consequence of attempts to increase energy density is to explore the possibility of drawing water from the surrounding ambience, using this property of

[4]Results presented in this chapter were published with Zhu et al. [43]

the fuels, so as to replace the space occupied by stoichiometric water with more on-board fuel. There are compelling reasons in favor of this approach. Firstly, we generate an exact quantity of water at the fuel cell cathode (besides losses limiting the electrochemical conversion efficiency) as that used to hydrolyse the fuel for generating the hydrogen, as shown by the balance of equations (4.1) with water molecules highlighted in blue. A method of recirculating this byproduct water from the cathode would replace stored water for hydrolysis.

$$MH_x + xH_2O \longrightarrow M(OH)_x + xH_2 \tag{4.1a}$$

$$xH_2 \longrightarrow 2xH^+ + 2xe^- \tag{4.1b}$$

$$xO_2 + 2xe^- + 2xH^+ \longrightarrow 2xOH^- \tag{4.1c}$$

$$xH_2 + \frac{x}{2}O_2 \longrightarrow xH_2O \tag{4.1d}$$

Secondly, there is additional water vapor from the ambient around the cathode available that can be passively drawn by the device for hydrolysis, and this can be driven by back diffusion through the nafion PEM in the presence of a strongly hygroscopic fuel. In net effect, the molarity of hydrogen production exactly matches the water stoichiometry for the reactions. Hence, if the fuel cell were started and all of the byproduct water from the cathode (along with some drawn from the ambient) be recycled to the fuel at the anode, the micro fuel cell should continue performing without the need for pumping additional water. The on-board fuel can thus be extended to replace all of the volume fraction occupied by the water reservoir, leading to much higher energy density as shown in table 4.1. The theoretical energy of all of the metal hydride fuels is now increased by ca. 100-150%. Some of these, exceeding 2000 Whr/L, are over four times the capacity of Li-ion battery systems [44].

4.3 The working concept behind the WRMFC

Consider a schematic of the WRMFC as shown in figure 4.1. The micro fuel cell can be divided into three functional parts: the nafion PEM, with a hydride fuel interfacing at the anode, and an air-breathing cathode. In this structure, the cathode along with the ambient humidity may be treated as the water vapor source for the microreactor/fuel cell. The device is said to work by *recovery* of water from the cathode through the MEA. The idea of such a water recovery has been employed earlier in the context of DMFCs in order to dilute the fuel to an operable concentration [45],[46],[47], but we alternatively propose this technique for driving the hydrolysis reaction. As shown in the figure, the dessicant hydride end is low in water vapor concentration

Hydrolysis reactions	Energy density w/ on-board water (Whr/L)	Energy density w/o on-board water (Whr/L)
$LiBH_4 + 4H_2O \longrightarrow H_3BO_3 + LiOH + 4H_2$	976	2163
$NaBH_4 + 4H_2O \longrightarrow H_3BO_3 + NaOH + 4H_2$	959	2080
$MgH_2 + 2H_2O \longrightarrow Mg(OH)_2 + 2H_2$	1054	2586
$LiH + H_2O \longrightarrow LiOH + H_2$	701	1157
$NaAlH_4 + 4H_2O \longrightarrow Al(OH)_3 + NaOH + 4H_2$	1044	2522
$LiAlH_4 + 4H_2O \longrightarrow Al(OH)_3 + LiOH + 4H_2$	1064	2645
$CaH_2 + 2H_2O \longrightarrow Ca(OH)_2 + 2H_2$	924	1920

Table 4.1: Theoretical energy density from hydrolysis of metal hydrides, at 0.6 V fuel cell operation

while the cathode is replete with byproduct water. This sets up a strong concentration gradient across the thin nafion PEM ($\leq$50 μm), and drives the flow of water vapor inside the PEM. The dynamic of this water vapor back-diffusion is governed by the affinity of the hydride for water, the ambient humidity, and the rate at which the produced hydrogen is consumed for the fuel cell reaction as this further determines the concentration of the byproduct water at the cathode.

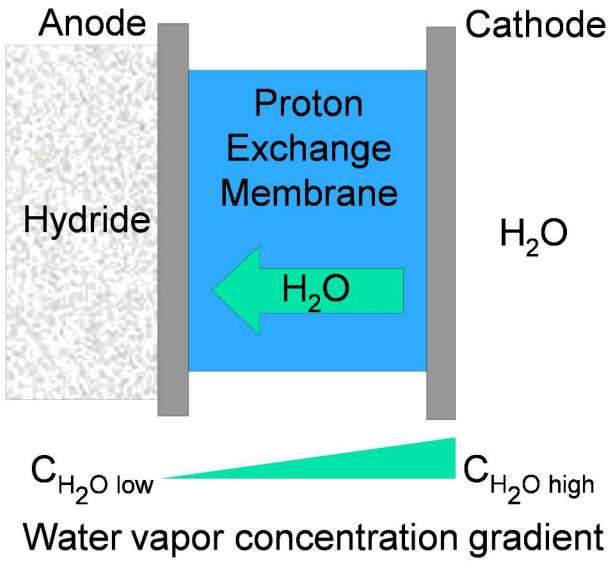

Figure 4.1: Operation scheme of a WRMFC, with hygroscopic metal hydride fuel, drawing water vapor for hydrolysis from cathode via back diffusion through the Nafion MEA

Back-diffusion of water vapor through the PEM ensures that the nafion membrane is continuously hydrated—an important condition for maintaining its porosity and proton conductivity [48],[49],[50]. However, the reverse direction of this process to that of charge transport sets up drag force that impedes both the proton conduction and the water vapor transport through the MEA. The device, although devoid of any on-board control mechanism, thus works in a self-regulating manner as dictated by the current generation and ambient humidity.

4.3.1 Designing the WRMFC

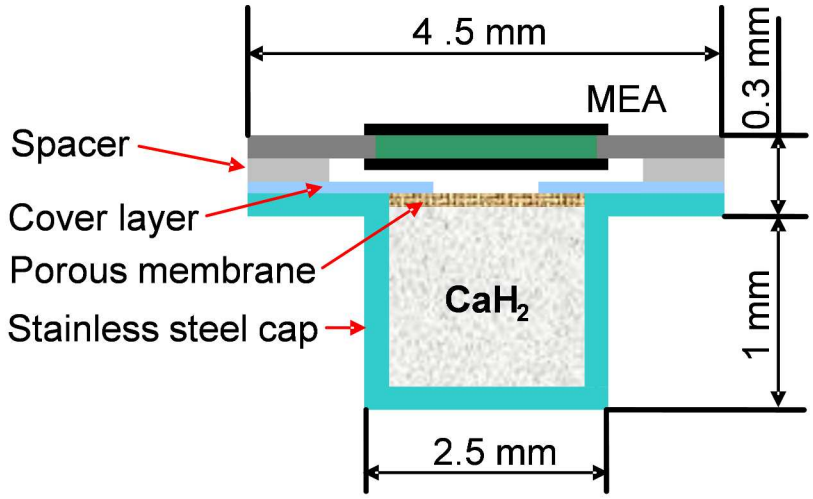

Figure 4.2: Schematic of the integrated water recovery micro fuel cell power generator

Figure 4.2 shows a schematic design of an integrated WRMFC device, based on the above concept. The device structure was simplified, and comprised of a hydride storage chamber/reactor with a cover layer supporting a hydrophobic PTFE membrane (to let water vapor diffuse through to the hydride), a miniaturized MEA that was fabricated as outlined in section 2.2.1, and a SS spacer between them. The spacer was accommodated in order to allow hydrogen build-up that could cater to periods of increased power demand. It also ensured that the MEA was not too close to the dessicant hydride, in order to prevent proton conductivity losses that could arise from complete dryout of nafion at the anode. A cylindrical form factor was chosen, in order to simplify alignment during assembly and epoxy bonding, and the device occupied 9.675 μL in volume. In comparison with the earlier design as shown in figure 2.5, the micro hydrogen generator accounted for ca. 50% of the fuel cell volume, with all of the increased storage for the hydride fuel.

4.4 Experimental testing of the WRMFC

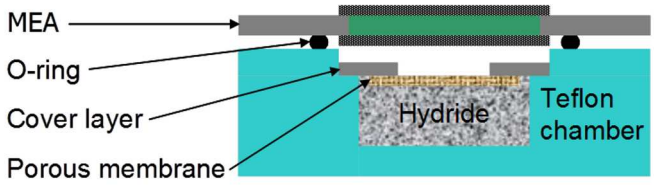

Figure 4.3: Schematic of a teflon testing package, with on-board hydride and MEA

WRMFC specimens were tested using a Solartron SI 1287 potentiostat. The devices were loaded with both CaH_2 and $LiAlH_4$ fuels to determine the effect of their properties on hydrogen generation within the WRMFC. Polarization and power density curves (figure 4.7) were drawn through potential stair-step experiments from short circuit to open circuit conditions. In order to observe mass transport limits at room condition, a polarization loop plot (figure 4.8) was also extracted by extending the potential stair-step procedure from open circuit to short circuit and back to open circuit conditions. AC impedance measurements were used to determine proton conductivity to study the effect of water transport mechanism on the PEM [48]. Lifetime testing of integrated WRMFCs was performed by extracting chronoamperograms in potentiostatic mode. Tests were performed at various relative humidity levels to simulate the effects on water recovery through the PEM, its effect on hydrogen generation, and MEA performance. A teflon testing package (figure 4.3) was assembled for this purpose. It comprised of a machined reaction chamber with a PTFE cover layer. An O-ring was used for hydrogen seal at the anode and the MEA was fastened on top. The MEA sizes, cover layer openings and fuel types could be changed in order to study their effects along with humidity. The package was also used to perform repeated polarization tests at various humidities.

4.4.1 Humidity controlled box

A humidity controlled box setup was designed in order to simulate different ambient humidity conditions for testing the WRMFC specimens. The humidity controlled box was supplied with air from two pressurized dry air cylinders and was fitted with a digital humidity-cum-temperature sensor (SHT75, Sensirion Inc., Switzerland) to monitor and record ambient conditions. One of the dry air streams was humidified by passing it through an air bubbler. Relative humidity inside the box was regulated by adjusting flow rates of the dry air and humidified air streams, both delivered to the box through a Tee-connector, based on humidity data recorded from the sensor. The box was vented, and operated in continuous flow mode to ensure that the ambient relative humidity was maintained uniformly around the WRMFC specimen.

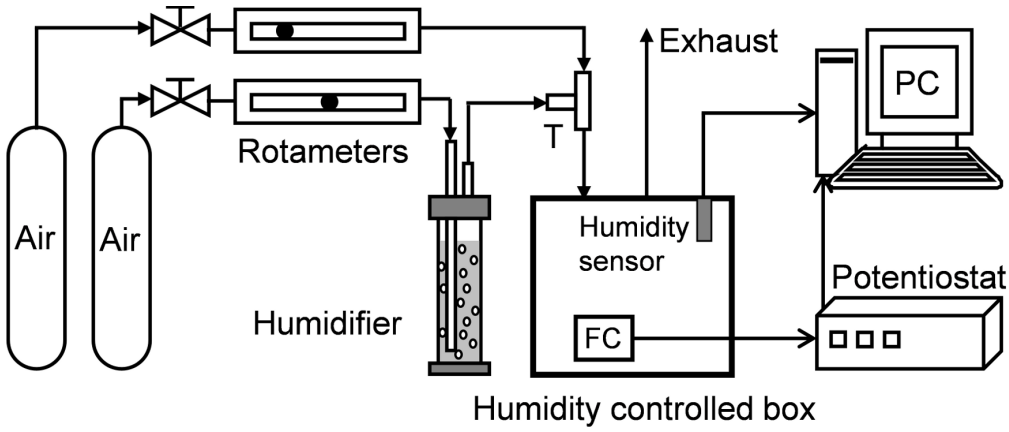

Figure 4.4: Schematic of the experimental WRMFC testing setup, with humidity control

4.5 Experimental Results

4.5.1 The effect of humidity

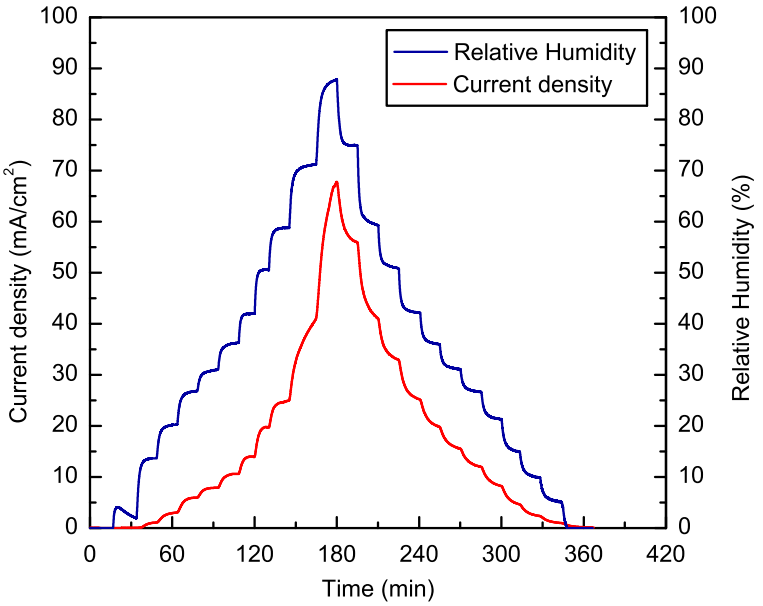

Figure 4.5: Variation of current density with time for the integrated WRMFC, by regulating humidity

Figure 4.5 shows a study of current density response to changes in ambient humidity. The device tested had an exposure area of 0.2 mm^3 through the cover layer for diffusion of water vapor to the hydride reactor. We observed that the WRMFC responsed quickly to changes in humidity around the cathode. Due to the size of the humidity controlled box and finite flow rates in controlling air streams to the box, the changes

weren't sharp. Rather, the ambient relative humidity took several minutes to asymptotically grow towards its steady state. The test was performed by both stepping-up the relative humidity from zero to a maximum of over 85% and further stepping-down back to zero in order to see directional dependance. During the entire period of the test lasting over 6 hours, the current density change tracked that of relative humidity and the performance did not drop significantly over time. Note that current density changes differ during the stepping up and stepping down processes. Initially slow, it changed sharply when the ambient relative humdity increase beyond 70%. While stepping-down, the current density changes were more gradual and the curve was less steep.

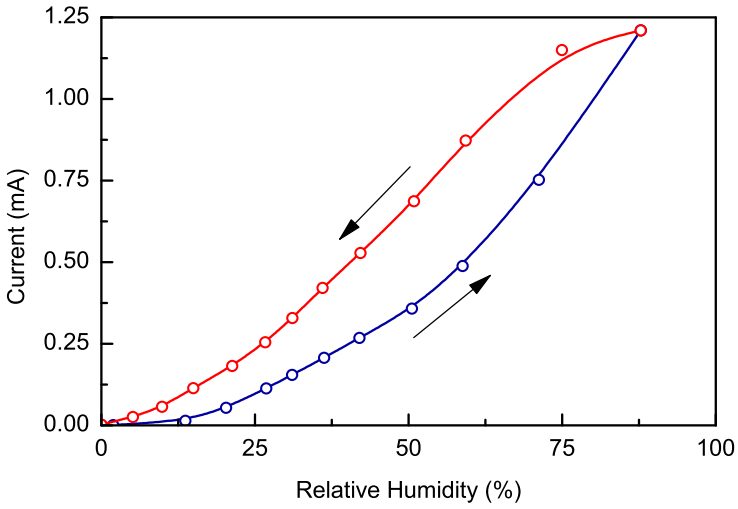

Figure 4.6: Variation of current with humidity for the integrated WRMFC

In order to observe this clearly, figure 4.6 has been extracted from the data and depicts current from the WRMFC with the direction of humidity increase (blue) and decrease (red). The path dependant behavior shows that the WRMFC's performance is strongly dependant on the initial condition of the cathode, i.e. whether the MEA was dry or hydrated prior to the humidity change. For example, consider a case of changing the ambient humidity between 50 and 75%. During the step-up direction the curent only increased from ca. 0.3-0.75 mA, whereas during step-down it was over 1.1 mA at 75% relative humidity and dropped to ca. 0.65 mA at 50% relative humidity. It is essentially an indicator of the availability of surrounding water vapor for hydrolysis, and hydrogen release that can be consumed to generate current.

The WRMFC is so sensitive to the ambience, it shows upto 50-100% variation between conditions of 30-75% relative humidity around the cathode. This strongly affects the performance, depending on the ambient relative humdity and also changes to it. The device would perform much better in humid climes.

4.5.2 Polarization and power density

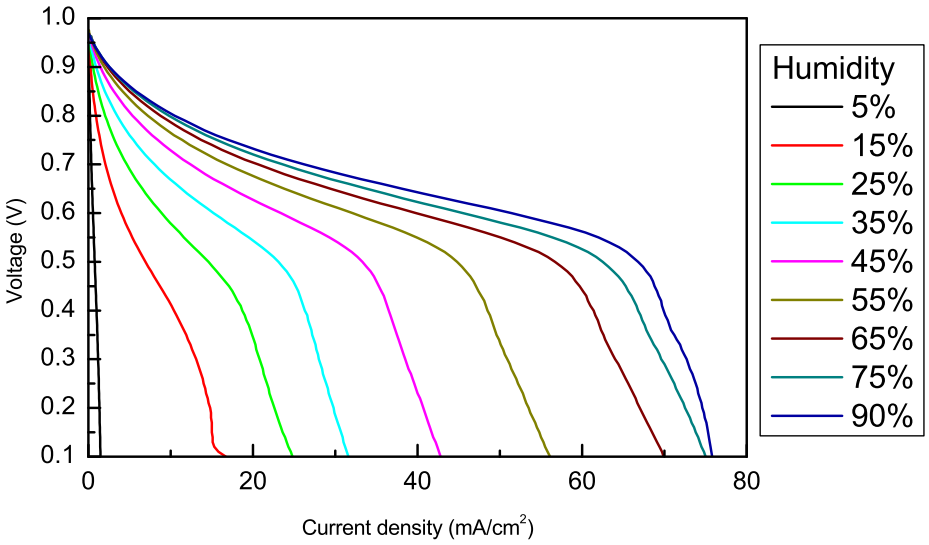

(a) Voltage versus current density

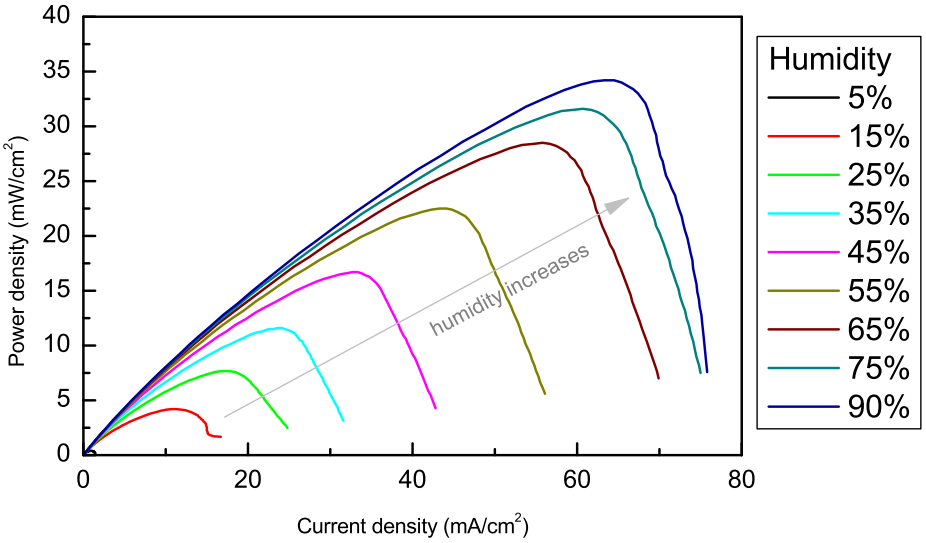

(b) Power density versus current density

Figure 4.7: Polarization and power density curves for the WRMFC, varying with humidity

Figure 4.7 shows polarization curves (from 0.1 V to open cell potential) of the WRMFC at nine different humidity levels from 5% to 90%. For clarity, the plot has been separated into two– figure 4.7(a) for voltages and figure 4.7(b) for power densities, both plotted against current density. The polarization curve at 5% relative humidity does not appear to have reached a hydrogen mass transport limit, unlike the others tests. At low ambient humidity ($\leq$25%), the device performance is poor. The current and power densties are very low due to lack of hydrogen (mass transport limit) and poor proton conductivity (low activation behavior) as

the byproduct water preferentially evaporates into the ambience. Dry ambience at the cathode and dessicant fuel at the anode pose severe limitation. The performance improves at intermediate humidities (35-65%). Here, the back-dffusion of water maintains both hydrogen generation and proton conductivity. Hence the current density increases and the device is able to deliver more power and sustain hydrogen generation. The maximum current density due to the mass transport limit increases by upto 200%. At very humid conditions, the micro fuel cell demonstrates further enhancement of power density but to a lesser extent. In this case, byproduct water and excess ambient moisture are fully available for back-diffusion to hydrolyse the fuel and generate more hydrogen. Although we expect improved current density by virtue of Nafion hydration driven by the large water concentration gradient, it is also accompanied by high ionic drag. This retards transfer of protons across the PEM and also affects hydrogen generation by slowing down water diffusion. Current and power density thus saturate.

The polarization plots above show that performance of the WRMFC is strongly affected by relative humidity, primarily because the byproduct water that is recovered and converted to hydrogen via hydrolysis reaction is related to the relative humidity. The relative humidity poses two competing effects- one, the byproduct water can be lost by evaporation into the ambient air when the relative humidity is low, and two, water vapor from ambient air also can diffuse backwards into the hydride chamber through the Nafion PEM. Only when an equilibrium is reached between these two effects, all of the byproduct water can exactly be recovered, and no additional water diffuses into the hydride chamber. However, the relative humidity can shift this equilibrium state and consequently affect the water diffusion rate through Nafion. The polarization plots show that whereas the WRMFC struggles at dry conditions and is better suited for high humidity, its performance shows vast spread at intermediate humidities and warrants tight control.

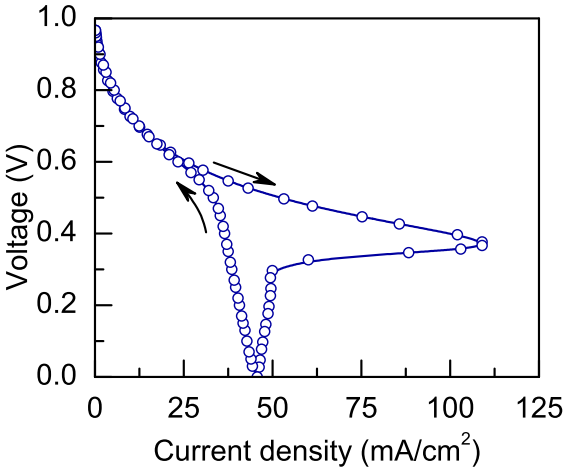

Figure 4.8: Polarization loop plot for the WRMFC at 45% relative humidity

A polarization loop plot (figure 4.8) was obtained for the WRMFC at 45% relative humidity conditions, by testing it in open air under the laboratory's natural ambience. Using this figure, we can establish appropriate operating voltages and switching actions for the device. From the test, we observed that the fuel cell had an activation region that extended to ca. 0.65 V. In this region, performance is impeded primarily by MEA dryout. Since the device is operating in low current mode, there is little water generated at the cathode due to which the kinetics and efficiency of the fuel cell reaction drop. However, there is accumulation of hydrogen in the space around the anode due to lack of consumption. The polarization curve extends further than hydrogen transport limit as we approach short crcuit. This is also briefly aided by increasing rate of hydrogen production and water back-diffusion as the current increases. Below 0.4 V, however, all of the excess hydrogen is fully consumed and the rate of hydrogen generation cannot keep up with consumption. At this point, the curve shifts backward, to *fully hydrogen mass transport limited* operation. During the reverse direction of testing, the curve follows a monotonic trend as it does not have accumulated hydrogen. This portion of the curve is an indicator of long-term current density at any given voltage. The device is fully hydrogen limited upto 0.5 V, and has a short ohmic region above that. At higher voltages ($\geq$0.7 V), it recovers activation behavior. The polarization plot of the WRMFC is similiar to the device with on-board water and microfluidic control (as discussed in section 3.5.1), but the current density is lower and mass transport limitations are more pronounced in comparison. We can take advantage of this behavior, when we switch to high-power regimes by dropping the operating voltage as it lasts for several seconds. While switching back to low power, the device quickly reaches higher voltage and conserves efficiency.

4.5.3 Humidity dependence of fuel cell parameters

Proton conductivity of the WRMFC and its variation with ambient humidity at 0.5 V operation is shown in figure 4.9. Whereas polarization curves provide the combined effect of both the MEA and hydrogen generation and its transport, this test is particularly useful to isolate the effects on the MEA that arise from humidity and how they affect device performance. It is well established that nafion hydration and water transport is crucial to maintaining fuel cell activity [48],[51]. At low ambient humidities ($\leq$25%), the proton conductivity of the WRMFC is low by 2-3 orders of magnitude and is indicative of both the dessicant effects of the hydride as well as byproduct water loss to the ambience. It increases as the humidity increases beacause the device shifts closer to the water transport equilibrium. The proton conductivity tends to saturate and plateau beyond 45% relative humidity. This matches with the current density trend of the fuel cell in polarization studies. While we expect that the device is not hydrogen mass transport limited at this voltage, the MEA faces impedance to charge transport despite increasing current density because of

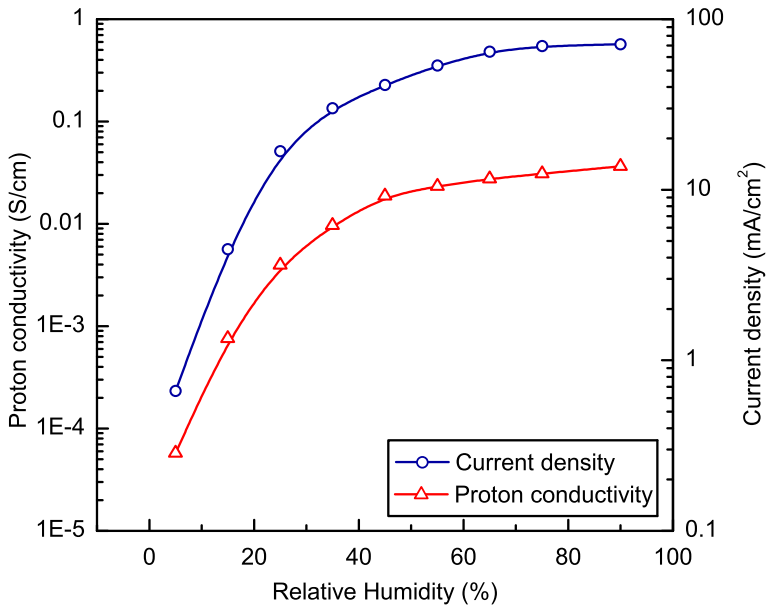

Figure 4.9: Proton conductivity and current density curves for the WRMFC, varying with humidity

the fact that increasing back-diffusion of water through Nafion causes strong electroosmotic drag. The ions, in turn, also slow down water diffusion towards the anode through the same force in the opposite direction [52],[53]. On the whole, the proton conductivity of the WRMFC, with a 25 μm thick Nafion 111 MEA is poorer than that of Nafion 117 [51]. Although the diffusion length and tortuosity of the PEM is reduced in our case, it is the dehydration from the strong dessicant hydride that impedes conductivity here. In order to overcome this while operating the WRMFC, higher ambient humdities ($\geq$45%) would be optimal from the point of view of maximizing proton conductivity and current density.

Figure 4.10 compares humidity behavior of the WRMFC over choice of fuels. CaH_2 and $LiAlH_4$ have already been established with better hydrogen evolution and kinetics among the hydrides (section 2.3). The plot shows that the device with $LiAlH_4$ has a higher performance at high relative humidities, but lower performance at lower humidities, compared to the device with CaH_2. This phenomenon can be explained by the powder size of these two hydrides. $LiAlH_4$ has a much smaller powder size than CaH_2, which implies larger exposed surface area to water vapor. At low relative humidity, the larger exposed area of the $LiAlH_4$ powder aggravates dessication to cause lower proton conductivity and dominates the performance of the fuel cell. At high relative humidities, it results in a higher hydrogen generation rate and increases the performance of the fuel cell. With CaH_2, the problem of byproduct expansion could also mean that it impedes further hydrolysis. If due allowance is given for this during fuel loading, then it could work to create larger openings and pathways for diffusion more water and enhancing hydrolysis.

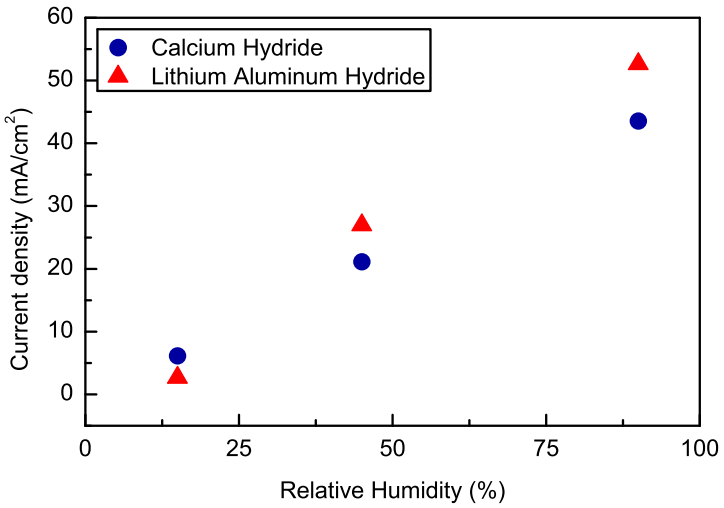

Figure 4.10: Performance variation of the WRMFC with humidity, for different fuels

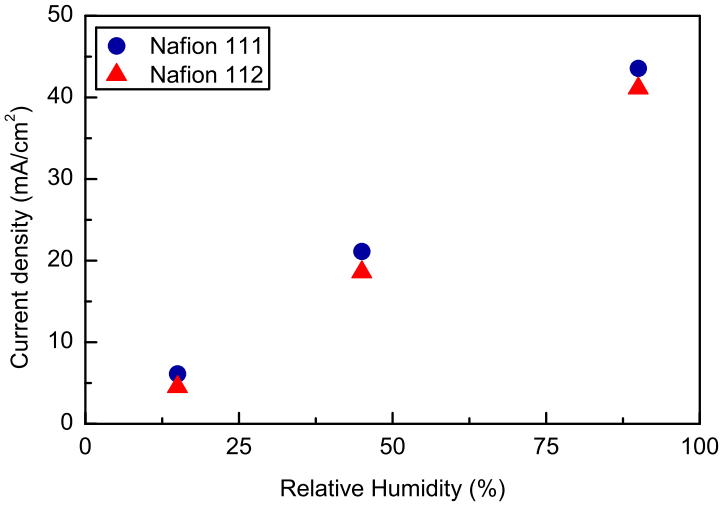

Figure 4.11: Performance variation of the WRMFC with humidity, for different Nafion thickness

The effect of PEM thickness on current density at 0.5 V, with respect to varying humidity, is shown for both Nafion 111 and Nafion 112 in figure 4.11. At all three points, Nafion 111 shows marginally better performance than Nafion 112. This could be due to improved hydrogen production in the former as the byproduct water has shorter diffusion path length. However the difference is not too significant, and this could be attributed to two reasons. Firstly, both of these membranes are equally affected by dryout effects. Secondly, the thickness of the catalyst layer (ca. 50 μm) could dominate over that of Nafion itself (25-50 μm). In net effect, PEM thickness is not a critical determinant but we choose the thicker Nafion 112 membrane for mechanical strength to withstand pressure shocks that could arise from hydrogen build-up at the anode.

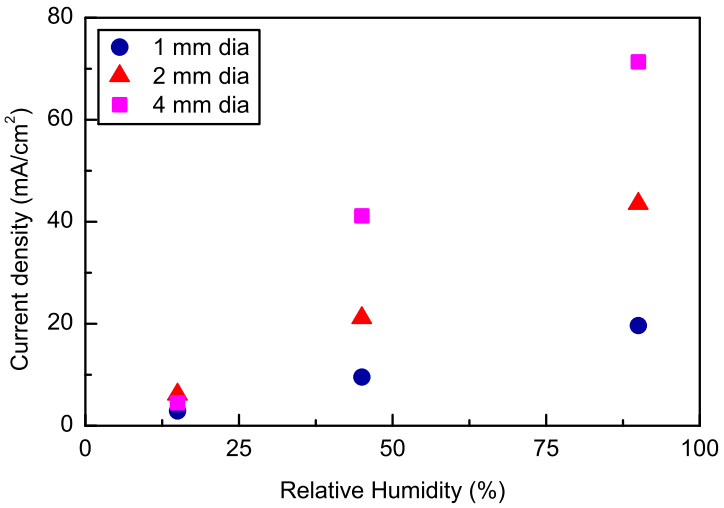

Figure 4.12: Performance variation of the WRMFC with humidity, for different opening areas

Figure 4.12 shows the performance of a WRMFC with three different opening areas in the cover layer: 1, 2, and 4 mm in diameter. The device with the largest opening has a higher performance at high relative humidity, but a lower performance at low humidity. At higher humidity, the larger area provides increased hydrogen production for current generation, but it is offset by electroosmotic drag at high current. Hence the increase in current density isn't proportional to the area. At low humidity, the larger exposed area to the hydride leads to low proton conductivity by dryout and this dominates fuel cell performance. However, current density is not proportional to the opening area, which shows that the opening area is not the only factor for the water diffusion through the Nafion membrane. Other factors, such as the area of the Nafion membrane and the distance between the Nafion and the hydride, also play important roles.

4.5.4 Lifetime performance tests

Lifetime performance of prototype integrated WRMFCs is depicted in the chronoamperograms in figure 4.13. Tests were performed on two 10 mm^3 devices with 0.2 mm^2 and 0.4 mm^2 opening areas on the cover layer, respectively. The ambient condition inside the humidity controlled box was maintained at a constant 50% relative humidity. Due to the extended activation region of the WRMFC, both these devices had to be operated in the mass transport limit region (0.5 and 0.6 V respectively). We observed that soon after beginning the test, the current density was at its maximum and it gradually decreased to zero in several hours over the progression of the tests. This corresponds to a maximum power density of 104 W/L, and the maximum energy density is 313 Whr/L. The burst of current was observed at the beginning because hydrogen was generated and pressurized inside the stainless steel cap while transferring the devices from

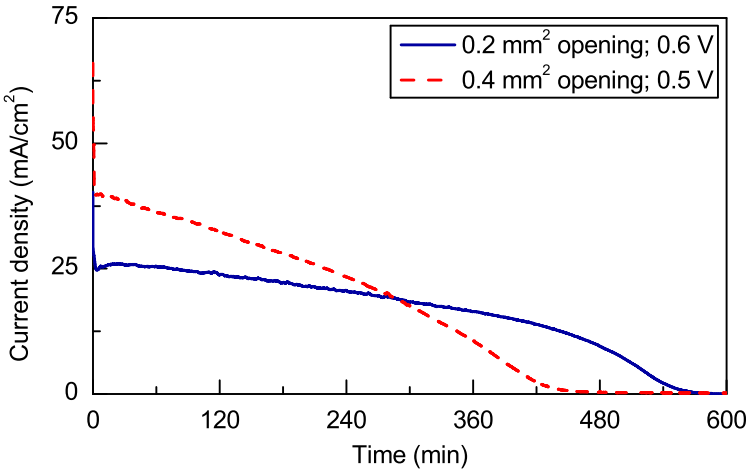

Figure 4.13: Chronoamperograms of integrated WRMFCs, showing variation with exposed area

dry glove box to the humidity controlled box. During this time, humidity around the cathode caused water to diffuse through and hydrolyse the CaH_2 fuel to produce excess hydrogen. After all of the accumulated hydrogen was consumed by the fuel cell and its levels fell below stoichiometric value, the current dropped, corresponding to hydrogen generation limits in the polarization curves (figure 4.7).

The shape of the WRMFC chronoamperogram, with continuous decay of current density over time is indicative of the fact that diffusion effects dominate device performance. While the devices operated over a period of 8-10 hours with hydrogen being generated, the byproduct hydroxide/hydrate from the hydrolysis reaction formed a barrier and increased the length over which water had to diffuse through the reactor to come in contact with fresh CaH_2 to produce more hydrogen. Hence the rate of hydrogen generation progressively decreased, driving the devices further into the hydrogen limited mode. Comparing the two devices, the 0.4 mm^2 device, by virtue of its larger opening area and lower operating voltage, delivered at higher power density than the 0.2 mm^2 device. However the latter had 16% more energy density because of operating with higher efficiency at 0.6 V. Operating in the hydrogen transport limited regime for higher current generation than at higher efficiencies near the activation region, means that we cannot entirely control the current density at constant voltage and the device output gradually declines while it reaches its full energy density.

The maximum energy density of 313 Whr/L for a WRMFC is reflective of the 38% volumetric ratio of fuel chamber to device, and is proportionately greater than the 200 Whr/L capacity of devices with on-board water (Chapter 3). However, it is still much lower than the theoretical estimated energy density of 740 Whr/L if the fuel chamber were completely filled with CaH_2 fuel. On one hand, it suggests incomplete

fuel hydrolysis due to mass transport limitations across reaction byproduct hydrate. Moreover in this work, the fuel chamber was not completely filled with hydride because the volume expansion of the hydride reactant to hydrate product (ca. 150% for CaH_2) can break the epoxy seals holding the chamber to the MEA. Some hydrogen loss may also accompany due to crossover through the thin MEA. In summary, the WRMFC concept is capable of enhancing the energy capacity of the micro fuel cell by over 33% and meet a peak power density goal of 100 W/L, but this occurs at the expense of our ability to switch power regimes and control the device for uniform power delivery. Such a device demonstrates diffusion dominated behavior that is strongly influenced by the ambient humidity.

Chapter 5

Conclusions

The goal of the micro power generator project was to develop a device that is 10 mm^3 in by volume and delivers upto 200 Whr/L energy density over a period of several of operation along with peak power density spikes of 100 W/L. Using the micro fuel cell concept, we have demonstrated prototype fully integrated devices that generate hydrogen on-board in microreactors and use it to produce current by running miniaturized MEAs. Prior research in micro fuel cells primarily focused on portable scale power generation by the use of liquid fuels and reforming techniques, and little on system integration. We have identified metal hydrides as highly concentrated sources with fast hydrogen release kinetics by spontaneous water hydrolysis reactions. Based on studies of their reaction rates and limiting factors such as byproduct volume expansions, we have designed and built suitable microreactors for the micro fuel cells. Among a variety of hydrides, both CaH_2 and $LiAlH_4$ based reactions have maximum hydrogen release and the fastest kinetics.

5.1 Implementation of control schemes

Two different approaches have been adopted for managing water transport and microfluidic control of the micro fuel cells. A passive water/liquid membrane-type microvalve in a hydrophilic channel, without the need for drawing parasitic power from the device itself, incorporates surface tension for pumping water to hydrolyse the fuel and supply hydrogen on-demand. The greatest advantage to implementing this method is the ability of the micro fuel cell to use hydrogen back pressure on the microvalve as feedback to self-regulate its power delivery in any given regime. While the microchannel and valve combination is able to pump water to overcome hydrogen mass transport limits and sustain nearly 400 W/L of peak power density for several seconds, the microvalve is also able to quickly switch and regulate hydrogen production for operating the fuel cell at higher voltage. By doing so, we extract maximum efficiency near the activation region during long periods of low current density and maximize the energy density of the device (200 Whr/L).

In contrast, the water recovery micro fuel cell entirely eliminates the need for carrying water and control mechanisms on-board. Relying on the hygroscopic property of the hydride fuels, the WRMFC draws

byproduct water at the cathode and humidity from the ambience via back-diffusion through the porous Nafion PEM for hydrogen generation. The benefit of simplifying the device design to only integrate the microreactor and the MEA is that we are able to allocate upto 38% of total device volume to more fuel on-board and this increases the energy density by upto 50% over the devices with microfluidic control and on-board water so as to deliver upto 313 Whr/L. While the WRMFC is devoid of any additional control scheme, its power delivery shows diffusion behavior. The performance is almost entirely dictated by water recovery across the MEA and ambient humidity—proton conductivity is the limiting factor at low humidity, while the water diffusion rate and electroosmotic drag affect the perfomance at high humidity.

5.2 Issues and challenges

The micro fuel cell concept worked satisfactorily to meet the goals of our project, but performance analysis of protoytpe devices has shown that their volumetric energy densities are two times lesser than theoretical expectations while designing them. Some of the challenges faced by the micro fuel cell are as follows:

a) The integrated micro fuel cells are typically hydrogen mass transport limited in operation. The rate of hydrogen generation, by diffusion of water vapor through membranes and porous fuel/byproduct beds prior to hydrolysis, is limited in comparison to running the device with hydrogen at excess pressure fed from a tank. Consequently, current density gradually decays over the lifetime.

b) Miniaturizing the MEA and operating at room temperature conditions, albeit prevention of surface heat transfer losses, limits the efficiency of Nafion-based PEMFCs that are known to perform best at 80°C temperatures.

c) Small form factors of device components means additional losses. Hydrogen is particularly hard to store and contain, in comparison with other gases, and it can easily leak from the integrated device through its components, seals and also via crossover through the PEM.

d) The physical state of hydride fuels poses handling issues while loading. Although our estimates of volumetric hydrogen release and energy densities beat the capacities of microbatteries and match up well against liquid fuels, their incorporation in a device is reduced by 17-186% because of volume expansion. The nature of the byproduct hydroxides and hydrates is such, the hydrolysis reaction cannot reach completion.

e) Performance is strongly dependent on ambient humidity, although the device with microvalve can offset this to some extent. The humidity strongly dictates limitations on proton conductivity and mass

transport, both of which are crucial to MEA performance and hydrogen generation.

f) Prototype devices built for this concept are for single use. After hydrolysis has completed and maximum energy achieved, the MEA remains capable of producing electricity if removed and supplied with a hydrogen source. While Pt-based catalyst ink is expensive, the device lacks reusability or regeneration.

5.3 Outlook and future directions

Despite stiff implementation challenges, the micro fuel cell power generator is able to integrate micro hydrogen generators, miniaturized MEAs and efficient microfluidic control schemes to deliver high energy densities in combination with high peak power densities. At the 10 μL size scales, such a combination of both high energy and power densities is a challenge faced by all methods including energy harvesting, batteries and ultracapacitors. Towards that, we have shown this concept to be capable of meeting targets. Along the way, we have also identified factors that critically affect integration and system performance.

There is scope for opportunities to overcome limitations encountered by the micro fuel cell power generators. The single largest factor to maximizing the capacity is the volumetric packing fraction of the fuel. The micro fuel cell can exceed energy densities of 1000 Whr/L by designing to accommodate $\geq$50% by volume of fuel on-board and minimizing the size of other components that do not contribute to the energy density, viz., the chambers, spacers, control layers and MEA. By designing and optimizing the fuel into a modular form factor (cartridges, for e.g.), energy and power density can be enhanced by improved kinetics of hydrolysis and reaction completion. The MEA could also be made reusable, which would in-turn make this concept cost-effective. Other enhancements could include self-hydration schemes to improve proton conductivity and water transport against humidity variations, particularly in the case of WRMFCs. Improved bonding schemes and seals can minimize hydrogen losses from the device.

The outlook for microscale power generators is optimistic. Miniaturizing more and more systems has been accompanied by further increasing energy demands at higher densities, and this is the driving agent behind energy generation by several methods at these scales. Newer materials with higher capacity and rates are being synthesized for battery electrodes; micro energy harvesters are being tuned to enhance their energy scavenging capabilites at lower frequencies and smaller temperature differences; and with improving bulk synthesis techniques, ultracapacitors are scaling-up better to higher volumetric energy densities. Amidst these methods the micro fuel cell, with the option of integrating high capacity metal hydride hydrogen sources and passive control schemes onto high-efficiency miniaturized MEAs, shows much promise to evolve into a solution for on-board power needs of microsystems.

References

[1] J. D. Morse, "Micro-fuel cell power sources," *International Journal of Energy Research*, vol. 31, pp. 576–602, 2007.

[2] A. Kundu, J. H. Jang, J. H. Gil, C. R. Jung, H. R. Lee, S. Kim, B. Ku, and Y. S. Oh, "Micro-fuel cells—Current development and applications," *Journal of Power Sources*, vol. 170, pp. 67–78, 2007.

[3] B. Kang and G. Ceder, "Battery materials for ultrafast charging and discharging," *Nature*, vol. 458, pp. 190–193, 2009.

[4] P. Notten, F. Roozeboom, R. Niessen, and L. Baggetto, "3-D Integrated All-Solid-State Rechargeable Batteries," *Advanced Materials*, vol. 19, no. 24, pp. 4564–4567, 2007.

[5] P. P. Prosini and P. Gislon, "A hydrogen refill for cellular phone," *Journal of Power Sources*, vol. 161, pp. 290–293, 2006.

[6] A. V. Pattekar and M. V. Kothare, "A Microreactor for Hydrogen Production in Micro Fuel Cell Applications," *Journal of Microelectromechanical Systems*, vol. 13, no. 1, pp. 7–18, 2004.

[7] B. Viswanathan and M. Aulice Scibioh, *Fuel Cells: Principles and Applications*. Hyderabad (India): Universities Press, first ed., 2007.

[8] P. Costamagna and S. Srinivasan, "Quantum jumps in the PEMFC science and technology from the 1960s to the year 2000 Part I. Fundamental scientific aspects," *Journal of Power Sources*, vol. 102, pp. 242–252, 2001.

[9] P. Costamagna and S. Srinivasan, "Quantum jumps in the PEMFC science and technology from the 1960s to the year 2000 Part II. Engineering, technology development and application aspects," *Journal of Power Sources*, vol. 102, pp. 253–269, 2001.

[10] J. Yeom, G. Z. Mozsgai, B. R. Flachsbart, E. R. Choban, A. Asthana, M. A. Shannon, and P. J. A. Kenis, "Microfabrication and characterization of a silicon-based millimeter scale, PEM fuel cell operating with hydrogen, methanol, or formic acid," *Sensors and Actuators B: Chemical*, vol. 107, no. 2, pp. 882 – 891, 2005.

[11] R. S. Jayashree, L. Gancs, E. R. Choban, A. Primak, D. Natarajan, L. J. Markoski, and P. J. A. Kenis, "Air-Breathing Laminar Flow-Based Microfluidic Fuel Cell," *Journal of the American Chemical Society*, vol. 127, no. 48, pp. 16758–16759, 2005.

[12] M. Mikkola, "Fuel Cells - An Overview." `http://www.tkk.fi/Units/AES/projects/renew/fuelcell/fc_index.html`, 2007. Helsinki University of Technology.

[13] B. R. Flachsbart, K. Wong, J. M. Iannacone, E. N. Abante, R. L. Vlach, P. A. Rauchfuss, P. W. Bohn, J. V. Sweedler, and M. A. Shannon, "Design and fabrication of a multilayered polymer microfluidic chip with nanofluidic interconnects via adhesive contact printing," *Lab on a Chip*, vol. 6, pp. 667–674, 2006.

[14] B. Gurau, L. Zhu, H. S. Kim, R. D. Morgan, V. V. Swaminathan, M. A. Shannon, and R. I. Masel, "Integrated Miniature Fuel Cell - Hydrogen Generator for Portable Power Generation," *ECS Meeting Abstracts*, vol. 802, no. 9, pp. 705–705, 2008.

[15] J. Yu, P. Cheng, Z. Ma, and B. Yi, "Fabrication of miniature silicon wafer fuel cells with improved performance," *Journal of Power Sources*, vol. 124, no. 1, pp. 40 – 46, 2003.

[16] D. Modroukas, V. Modi, and F. L. G, "Micromachined silicon structures for free-convection PEM fuel cells," *Journal of Micromechanics and Microengineering*, vol. 15, pp. 193 – 201, 2005.

[17] J. P. Meyers and H. L. Maynard, "Design considerations for miniaturized PEM fuel cells," *Journal of Power Sources*, vol. 109, pp. 76–88, 2002.

[18] Z. Xiao, G. Yan, C. Feng, P. C. H. Chan, and I.-M. Hsing, "A silicon-based fuel cell micro power system using a microfabrication technique," *Journal of Micromechanics and Microengineering*, vol. 16, no. 10, p. 2014, 2006.

[19] T. Pichonat and B. Gauthier-manuel, "Mesoporous silicon-based miniature fuel cells for nomadic and chip-scale systems," *Microsystem Technologies*, vol. 12, no. 4, pp. 330–334, 2006.

[20] L. Zhu, D. Kim, H. Kim, R. I. Masel, and M. A. Shannon, "Hydrogen generation from hydrides in millimeter scale reactors for micro proton exchange membrane fuel cell applications," *Journal of Power Sources*, vol. 185, no. 2, pp. 1334 – 1339, 2008.

[21] R. Aiello, M. A. Matthews, D. L. Reger, and J. E. Collins, "Production of hydrogen gas from novel chemical hydrides," *International Journal of Hydrogen Energy*, vol. 23, no. 12, pp. 1103 – 1108, 1998.

[22] B. Sakintuna, F. Lamari-Darkrim, and M. Hirscher, "Metal hydride materials for solid hydrogen storage: A review," *International Journal of Hydrogen Energy*, vol. 32, no. 9, pp. 1121–1140, 2007.

[23] P. Muthukumar, M. P. Maiya, and S. S. Murthy, "Experiments on a metal hydride-based hydrogen storage device," *International Journal of Hydrogen Energy*, vol. 30, no. 15, pp. 1569 – 1581, 2005.

[24] F. L. Darkrim, P. Malbrunot, and G. P. Tartaglia, "Review of hydrogen storage by adsorption in carbon nanotubes," *International Journal of Hydrogen Energy*, vol. 27, no. 2, pp. 193 – 202, 2002.

[25] C. Liu, Y. Y. Fan, M. Liu, H. T. Cong, H. M. Cheng, and M. S. Dresselhaus, "Hydrogen Storage in Single-Walled Carbon Nanotubes at Room Temperature," *Science*, vol. 286, no. 5442, pp. 1127–1129, 1999.

[26] A. C. Dillon, K. M. Jones, T. A. Bekkedahl, C. H. Kiang, D. S. Bethune, and M. J. Heben, "Storage of hydrogen in single-walled carbon nanotubes," *Nature*, vol. 386, pp. 377–379, 1997.

[27] N. L. Rosi, J. Eckert, M. Eddaoudi, D. T. Vodak, J. Kim, M. O'Keeffe, and O. M. Yaghi, "Hydrogen Storage in Microporous Metal-Organic Frameworks," *Science*, vol. 300, no. 5622, pp. 1127–1129, 2003.

[28] M. Ni, D. Y. C. Leung, and M. K. H. Leung, "A review on reforming bio-ethanol for hydrogen production," *International Journal of Hydrogen Energy*, vol. 32, no. 15, pp. 3238 – 3247, 2007.

[29] M. J. Varady, L. McLeod, J. M. Meacham, F. L. Degertekin, and A. G. Fedorov, "An integrated MEMS infrastructure for fuel processing: hydrogen generation and separation for portable power generation," *Journal of Micromechanics and Microengineering*, vol. 17, no. 9, p. S257, 2007.

[30] U.S. DOE Fuel Cell Technologies Program, "Multi-Year Research, Development and Demonstration Plan: Planned Program Activities for 2005-2015," tech. rep., U.S. Department of Energy, 2003. `http://www1.eere.energy.gov/hydrogenandfuelcells/resources.html`.

[31] J. Yeom, I. Oh, C. Field, A. Radadia, Z. Ni, B. Bae, J. Han, R. I. Masel, and M. A. Shannon, "Enhanced toxic gas detection using a MEMS preconcentrator coated with the metal organic framework absorber," in *IEEE 21st International Conference on Micro Electro Mechanical Systems*, (Tucson, AZ), pp. 232–235, 2008.

[32] V. C. Y. Kong, F. R. Foulkes, D. W. Kirk, and J. T. Hinatsu, "Development of hydrogen storage for fuel cell generators I: Hydrogen generation using hydrolysis hydrides," *International Journal of Hydrogen Energy*, vol. 24, pp. 665–675, 1999.

[33] V. C. Y. Kong, D. W. Kirk, F. R. Foulkes, and J. T. Hinatsu, "Development of hydrogen storage for fuel cell generators II : utilization of calcium hydride and lithium hydride," *International Journal of Hydrogen Energy*, vol. 28, pp. 205 – 214, 2003.

[34] J. Tessier, J. Huot, R. Schulz, and D. Guay, "Hydrogen production and crystal structure of ball-milled MgH_2–Ca and MgH_2–CaH_2 mixtures," *Journal of Alloys and Compounds*, vol. 376, pp. 180–185, 2004.

[35] G. K. Pitcher and G. J. Kavarnos, "A test assembly for hydrogen production by the hydrolysis of solid lithium hydride," *International Journal of Hydrogen Energy*, vol. 22, no. 6, pp. 575–579, 1997.

[36] Y. Kojima, K.-I. Suzuki, and Y. Kawai, "Hydrogen generation by hydrolysis reaction of magnesium hydride," *Journal of Materials Science*, vol. 39, no. 2, pp. 2227 – 2229, 2004.

[37] V. V. Swaminathan, L. Zhu, B. Gurau, R. I. Masel, and M. A. Shannon, "A Micro Hydrogen Generator with a Microfluidic Self-Regulating Valve for Sensors and Fuel Cells," in *IEEE 22nd International Conference on Micro Electro Mechanical Systems*, (Sorrento, Italy), pp. 35 –38, 2009.

[38] S. Timoshenko and S. Woinowsky-Krieger, *Theory of Plates and Shells*. New York: McGraw-Hill, second ed., 1959.

[39] M. T. A. Saif, B. E. Alaca, and H. Sehitoglu, "Analytical modeling of electrostatic membrane actuator for micro pumps," *Journal of Microelectromechanical Systems*, vol. 8, no. 3, pp. 335–345, 1999.

[40] J. C. Selby, M. A. Shannon, K. Xu, and J. Economy, "Sub-micrometer solid-state adhesive bonding with aromatic thermosetting copolyesters for the assembly of polyimide membranes in silicon-based devices," *Journal of Micromechanics and Microengineering*, vol. 11, no. 6, pp. 672–685, 2001.

[41] G. M. Walker and D. J. Beebe, "A passive pumping method for microfluidic devices.," *Lab on a chip*, vol. 2, no. 3, pp. 131–134, 2002.

[42] D.-H. Eom, G.-B. Lim, J.-G. Park, and A. A. Busnaina, "Reaction of Ozone and H_2O_2 in NH_4OH Solutions and Their Reaction with Silicon Wafers," *Japanese Journal of Applied Physics*, vol. 43, pp. 3335–3339, June 2004.

[43] L. Zhu, V. Swaminathan, B. Gurau, R. Masel, and M. Shannon, "An onboard hydrogen generation method based on hydrides and water recovery for micro-fuel cells," *Journal of Power Sources*, vol. 192, no. 2, pp. 556 – 561, 2009.

[44] R. Hahn, "Status of Existing Technologies," in *Hydrogen Technology: Mobile and Portable Applications* (A. Léon, ed.), Green Energy and Technology, pp. 381–408, Springer Berlin Heidelberg, 2008.

[45] R. Jiang and D. Chu, "Water Crossover: A Challenge to DMFC System I. Experimental Determination of Water Crossover," *Journal of The Electrochemical Society*, vol. 155, no. 8, pp. B798–B803, 2008.

[46] H. Kim, J. Oh, J. Kim, and H. Chang, "Membrane electrode assembly for passive direct methanol fuel cells," *Journal of Power Sources*, vol. 162, no. 1, pp. 497 – 501, 2006.

[47] S.-C. Yao, X. Tang, C.-C. Hsieh, Y. Alyousef, M. Vladimer, G. K. Fedder, and C. H. Amon, "Micro-electro-mechanical systems (MEMS)-based micro-scale direct methanol fuel cell development," *Energy*, vol. 31, no. 5, pp. 636 – 649, 2006.

[48] T. E. Springer, T. A. Zawodzinski, and S. Gottesfeld, "Polymer Electrolyte Fuel Cell Model," *Journal of The Electrochemical Society*, vol. 138, no. 8, pp. 2334–2342, 1991.

[49] S. Motupally, A. J. Becker, and J. W. Weidner, "Diffusion of Water in Nafion 115 Membranes," *Journal of The Electrochemical Society*, vol. 147, no. 9, pp. 3171–3177, 2000.

[50] S. Slade, S. A. Campbell, T. R. Ralph, and F. C. Walsh, "Ionic Conductivity of an Extruded Nafion 1100 EW Series of Membranes," *Journal of The Electrochemical Society*, vol. 149, no. 12, p. A1556, 2002.

[51] Y. Sone, P. Ekdunge, and D. Simonsson, "Proton Conductivity of Nafion 117 as Measured by a Four-Electrode AC Impedance Method," *Journal of The Electrochemical Society*, vol. 143, no. 4, pp. 1254–1259, 1996.

[52] Z. W. Dunbar and R. I. Masel, "Quantitative MRI study of water distribution during operation of a PEM fuel cell using Teflon® flow fields," *Journal of Power Sources*, vol. 171, no. 2, pp. 678 – 687, 2007.

[53] Z. W. Dunbar and R. I. Masel, "Magnetic resonance imaging investigation of water accumulation and transport in graphite flow fields in a polymer electrolyte membrane fuel cell: Do defects control transport?," *Journal of Power Sources*, vol. 182, no. 1, pp. 76 – 82, 2008.

[54] L. Zhu, K. Lin, R. Morgan, V. V. Swaminathan, H. Kim, B. Gurau, D. Kim, B. Bae, R. Masel, and M. Shannon, "Integrated micro-power source based on a micro-silicon fuel cell and a micro electromechanical system hydrogen generator," *Journal of Power Sources*, vol. 185, no. 2, pp. 1305 – 1310, 2008.

[55] S. Moghaddam, E. Pengwang, K. Lin, R. Masel, and M. Shannon, "Millimeter-Scale Fuel Cell With Onboard Fuel and Passive Control System," *Microelectromechanical Systems, Journal of*, vol. 17, no. 6, pp. 1388 –1395, 2008.

[56] K.-L. Chu, S. Gold, V. Subramanian, C. Lu, M. Shannon, and R. Masel, "A Nanoporous Silicon Membrane Electrode Assembly for On-Chip Micro Fuel Cell Applications," *Journal of Microelectromechanical Systems*, vol. 15, no. 3, pp. 671–677, 2006.

[57] K.-L. Chu, M. A. Shannon, and R. I. Masel, "An Improved Miniature Direct Formic Acid Fuel Cell Based on Nanoporous Silicon for Portable Power Generation," *Journal of The Electrochemical Society*, vol. 153, no. 8, pp. A1562–A1567, 2006.

[58] S. Moghaddam, E. Pengwang, R. Masel, and M. Shannon, "A self-regulating hydrogen generator for micro fuel cells," *Journal of Power Sources*, vol. 185, no. 1, pp. 445–450, 2008.

[59] K. Williams and R. Muller, "Etch Rates for Micromachining Processing," *Journal of Microelectromechanical Systems*, vol. 5, no. 4, pp. 256–269, 1996.

[60] K. Williams, K. Gupta, and M. Wasilik, "Etch Rates for Micromachining Processing-Part II," *Journal of Microelectromechanical Systems*, vol. 12, no. 6, pp. 761–778, 2003.

[61] G. T. A. Kovacs, N. I. Maluf, and K. E. Petersen, "Bulk micromachining of silicon," *Proceedings of the IEEE*, vol. 86, no. 8, pp. 1536 –1551, 1998.

[62] K. W. Oh and C. H. Ahn, "A review of microvalves," *Journal of Micromechanics and Microengineering*, vol. 16, no. 5, pp. R13–R39, 2006.

[63] A. Rowe and X. Li, "Mathematical modeling of proton exchange membrane fuel cells," *Journal of Power Sources*, vol. 102, pp. 82–96, 2001.

[64] T. V. Nguyen and R. E. White, "A Water and Heat Management Model for Proton-Exchange-Membrane Fuel Cells," *Journal of The Electrochemical Society*, vol. 140, no. 8, pp. 2178–2186, 1993.

[65] G.-D. J. Su, Y. W. Yeh, C.-W. E. Chiu, C.-H. Li, and T.-Y. Chen, "Fabrication and Measurement of Low-Stress Polyimide Membrane for High-Resolution Variable Optical Attenuator," *Selected Topics in Quantum Electronics, IEEE Journal of*, vol. 13, no. 2, pp. 312 –315, 2007.

[66] H. J. Kook and D. Kim, "In situ measurements and analysis of imidization extent, thickness, and stress during the curing of polyimide films," *Journal of Materials Science*, vol. 35, pp. 2949–2954, 2000.

[67] S. Gold, "Acid loaded porous silicon as a proton exchange membrane for micro-fuel cells," *Journal of Power Sources*, vol. 135, pp. 198–203, 2004.

[68] E.-D. Wang, P.-F. Shi, and C.-Y. Du, "A novel self-humidifying membrane electrode assembly with water transfer region for proton exchange membrane fuel cells," *Journal of Power Sources*, vol. 175, pp. 183–188, 2008.

[69] X. Zhu, H. Zhang, Y. Zhang, Y. Liang, X. Wang, and B. Yi, "An ultrathin self-humidifying membrane for PEM fuel cell application: fabrication, characterization, and experimental analysis.," *The Journal of Physical Chemistry B*, vol. 110, no. 29, pp. 14240–14248, 2006.